

Supporting Information

Understanding and optimizing ultra-thin coordination polymer derivatives with high oxygen evolution performance

Yonggui Zhao,[‡] Wenchao Wan,[‡] Yi Chen, Rolf Erni, C. A. Triana, Jingguo Li, Christos K. Mavrokefalos, Ying Zhou and Greta R. Patzke*

Y. G. Zhao, W. C. Wan, Dr. C. A. Triana, J. G. Li, Dr. C. K. Mavrokefalos, and Prof. G. R. Patzke
Department of Chemistry, University of Zurich, Winterthurerstrasse 190, CH-8057 Zurich, Switzerland
E-mail: greta.patzke@chem.uzh.ch

Y. Chen and Prof. Y. Zhou

State Key Laboratory of Oil and Gas Reservoir and Exploitation and The Center of New Energy Materials and Technology, School of New Energy and Materials, Southwest Petroleum University, Chengdu 610500, China

Dr. R. Erni

Electron Microscopy Center, Empa, Swiss Federal Laboratories for Materials Science and Technology, Überlandstrasse 129, CH-8600 Dübendorf, Switzerland

[‡]Y. G. Zhao and W. C. Wan contributed equally to this work.

*Corresponding author

Table of Contents

Experimental details and methods	S4
Figure S1. Theoretical and experimental PXRD patterns of Ni _{10-x} Fe _x -CPs	S9
Figure S2. FTIR spectra of Ni _{10-x} Fe _x -CPs	S9
Figure S3. Raman spectra of Ni _{10-x} Fe _x -CPs.....	S9
Figure S4. FESEM images of Ni _{10-x} Fe _x -CPs	S10
Figure S5. FESEM-EDX spectra images of Ni _{10-x} Fe _x -CPs	S11
Figure S6. FESEM-EDX elemental mappings of Ni _{10-x} Fe _x -CPs.....	S12
Figure S7. PXRD patterns of R-Ni _{10-x} Fe _x -CPs.....	S12
Figure S8. FESEM images of R-Ni _{10-x} Fe _x -CPs	S13
Figure S9. TEM images of R-Ni _{10-x} Fe _x -CPs	S14
Figure S10. FESEM-EDX elemental mappings of R-Ni _{10-x} Fe _x -CPs.....	S15
Figure S11. FESEM-EDX spectra of R-Ni _{10-x} Fe _x -CPs.....	S16
Figure S12. PXRD pattern of NiFe-LDH	S17
Figure S13. FESEM and TEM images of NiFe-LDH	S17
Figure S14. FESEM-EDX spectrum and elemental mappings of NiFe-LDH	S18

Figure S15. PXRD pattern of NiFe-oxides.....	S18
Figure S16. FESEM and TEM images of NiFe-oxides.....	S19
Figure S17. FESEM-EDX spectrum and elemental mappings of NiFe-oxides.....	S19
Figure S18. PXRD pattern of R-NiFe-NPs	S20
Figure S19. FESEM and TEM images of R-NiFe-NPs.....	S20
Figure S20. FESEM-EDX spectrum and elemental mappings of R-NiFe-NPs.....	S21
Figure S21. Fitting of the Ni <i>K</i> -edge XAS data of reference Ni foil.....	S21
Figure S22. Schematic crystal structures of Ni _{10-x} Fe _x -CPs (<i>x</i> =0, 2, and 5).	S21
Figure S23. Ni <i>K</i> -edge XAS spectra of Ni _{10-x} Fe _x -CPs (<i>x</i> =0, 2, and 5) vs. reference.....	S22
Figure S24. Fitting of the Fe <i>K</i> -edge XAS data of reference Fe foil.....	S22
Figure S25. Fe <i>K</i> -edge XAS spectra of Ni _{10-x} Fe _x -CPs (<i>x</i> =2 and 5) vs. reference.....	S22
Figure S26. Ni <i>K</i> -edge XAS spectra of R-Ni _{10-x} Fe _x -CPs (<i>x</i> =0, 2, and 5) vs. reference.....	S23
Figure S27. Fitting of the Ni <i>K</i> -edge EXAFS $k^3\chi(k)$ spectra	S24
Figure S28. Fe <i>K</i> -edge XAS spectra of R-Ni _{10-x} Fe _x -CPs (<i>x</i> =2 and 5) vs. reference.....	S25
Figure S29. Fitting of the Fe <i>K</i> -edge XAS data of R-NiFe-CPs and NiFe-LDH	S26
Figure S30. Ni <i>K</i> -edge XAS spectra of NiFe-oxides vs. reference	S26
Figure S31. Fe <i>K</i> -edge XAS spectra of NiFe-oxides vs. reference	S27
Figure S32. Ni <i>K</i> -edge XAS spectra of R-NiFe-NPs vs. reference	S27
Figure S33. Fe <i>K</i> -edge XAS spectra of R-NiFe-NPs vs. reference	S28
Figure S34. XPS spectra of NiFe-CPs, R-NiFe-CPs, and NiFe-LDH.....	S28
Figure S35. High-resolution XPS spectra of N1s, Ni2p, and Fe 2p for NiFe-CPs.....	S28
Figure S36. High-resolution XPS spectra of B 1s for R-NiFe-CPs.....	S29
Figure S37. High-resolution XPS spectra of Fe 2p for R-NiFe-CPs and NiFe-LDH.....	S29
Figure S38. Electrocatalytic performance of Ni _{10-x} Fe _x -CPs and R-Ni _{10-x} Fe _x -CPs.....	S30
Figure S39. CV curves of R-NiFe-CPs before and after 90% iR correction	S31
Figure S40. Electrocatalytic performance of R-Ni _{10-x} Fe _x -CPs with different mass loadings	S31
Figure S41. ECSA measurements of R-Ni _{10-x} Fe _x -CPs (0≤ <i>x</i> ≤5).	S32
Figure S42. ECSA measurements of as-prepared catalysts.....	S33
Figure S43. CV curves and overpotentials at 1 mA/cm _{ECSA} ² of the six catalysts	S34
Figure S44. CV curves and overpotential at 10 mA/cm _{geometric} ² and 1 mA/cm _{ECSA} ² of the five catalysts.....	S34
Figure S45. Nyquist plots of the five catalysts.....	S35
Figure S46. Faradaic efficiency measurements of R-NiFe-CPs.....	S35
Figure S47. Chronoamperometric measurements of the five catalysts	S36
Figure S48. TEM images of post-catalytic of NiFe-CPs and R-NiFe-CPs	S37
Figure S49. XAS spectra of NiFe-CPs before and after OER measurements	S38
Figure S50. XAS spectra of R-NiFe-CPs before and after OER measurements	S39
Figure S51. Adsorption slab models of Ni-LDH.....	S40
Figure S52. Adsorption slab models of NiFe-LDH.....	S40
Figure S53. Adsorption slab models of R-NiFe-CPs	S40
Figure S54. Computed total DOS of Ni-LDH, NiFe-LDH, and R-NiFe-CPs	S41

Figure S55. CV curves of R-Ni _{1-x} Fe _x -CPs and Ni _{1-x} Fe _x -LDH.....	S41
Figure S56. Computed free energies of OER steps for Ni-LDH.....	S42
Figure S57. Computed free energies of OER steps for NiFe-LDH.....	S42
Figure S58. Computed free energies of OER steps for R-NiFe-CPs.....	S43
Figure S59. Randles-Sevcik and Laviron tests for Ni-LDH.....	S43
Figure S60. Randles-Sevcik and Laviron tests for Ni ₉ Fe ₁ -LDH	S44
Figure S61. Randles-Sevcik and Laviron tests for R-Ni ₉ Fe ₁ -CPs	S44
Figure S62. PXRD patterns of R-NiFe-CPs with 0.3 and 3.0 M of NaBH ₄	S44
Figure S63. FESEM and TEM images of R-NiFe-CPs with 0.3 and 3.0 M of NaBH ₄	S45
Figure S64. FESEM-EDX spectra of R-NiFe-CPs with 0.3 and 3.0 M of NaBH ₄	S46
Figure S65. FESEM-EDX elemental mappings of R-NiFe-CPs with 0.3 and 3.0 M of NaBH ₄	S46
Figure S66. Ni <i>K</i> -edge XAS spectra of R-NiFe-CPs with 0.3, 1.0, and 3.0 M of NaBH ₄	S47
Figure S67. Fe <i>K</i> -edge XAS spectra of R-NiFe-CPs with 0.3, 1.0, and 3.0 M of NaBH ₄	S47
Figure S68. Room temperature EPR spectra of R-NiFe-CPs with 0.3, 1.0, and 3.0 M of NaBH ₄	S47
Table S1. ICP-MS results: Ni/Fe ratio for the synthesis of NiFe-CPs.....	S48
Table S2. ICP-MS results: B and Na content for the synthesis of R-NiFe-CPs	S48
Table S3. ICP-MS results: purified 1 M KOH before and after OER measurements	S48
Table S4. Elemental analysis of NiFe-CPs and R-NiFe-CPs	S48
Table S5. FESEM-EDX and ICP-MS results of Ni/Fe ratio for the as-prepared catalysts.....	S48
Table S6. ICP-MS results: Ni/Fe ratio for the synthesis of R-NiFe-CPs.....	S48
Table S7. Fitting parameters of Ni <i>K</i> -edge EXAFS for the as-prepared catalysts and references.....	S49
Table S8. Fitting parameters of Fe <i>K</i> -edge EXAFS for the as-prepared catalysts and references.....	S50
Table S9. Comparison of OER performance of as-prepared catalysts with recent representative works on NiFe-based OER electrocatalysts.....	S51
Table S10. Comparison of OER performance of the as-prepared catalysts with recent representative works on ultra-thin based OER electrocatalysts.	S52
References	S53

Experimental Details and Methods

Chemicals. Nickel(II) chloride ($\geq 98\%$), nickel(II) nitrate hexahydrate ($\geq 99.999\%$), iron(II) chloride tetrahydrate ($\geq 99\%$), iron(III) nitrate nonahydrate ($\geq 99.99\%$), potassium tetracyanonickelate(II) hydrate ($\geq 99\%$), potassium hydroxide ($\geq 99.97\%$), sodium borohydride ($\geq 98\%$), trisodium citrate dehydrate ($\geq 99\%$), and urea ($\geq 98\%$) were purchased from Sigma-Aldrich. All chemicals were used as received without any further purification.

Synthesis of $\text{Ni}_{10-x}\text{Fe}_x\text{-CPs}$ ($0 \leq x \leq 5$). As a representative example, Ni-CPs were prepared as follows. 0.4 mmol of nickel(II) chloride and 0.3 mmol of trisodium citrate dehydrate were dissolved into 20 ml of deionized (DI) water to form a clear transparent green solution A. At the same time, a total of 0.4 mmol of potassium tetracyanonickelate(II) was added into 20 mL of DI water to form a clear transparent solution B. Solution B was rapidly injected into solution A under magnetic stirring for 3 min. The mixture was kept at room temperature for another 24 h. The as-synthesized Ni-CPs were centrifuged and washed with DI water and ethanol several times. The products were dried at $70\text{ }^\circ\text{C}$ overnight before use. Fe-doped Ni-CPs were synthesized by the same strategy applied for Ni-CPs, except that additional iron(II) chloride tetrahydrate was dissolved into solution A. The Ni-CPs with different amounts of Fe doping were denoted as $\text{Ni}_9\text{Fe}_1\text{-CPs}$, $\text{Ni}_8\text{Fe}_2\text{-CPs}$ (referred to NiFe-CPs), $\text{Ni}_7\text{Fe}_3\text{-CPs}$, $\text{Ni}_6\text{Fe}_4\text{-CPs}$, and $\text{Ni}_5\text{Fe}_5\text{-CPs}$, respectively, indicating the applied starting ratios.

Synthesis of reductive $\text{Ni}_{10-x}\text{Fe}_x\text{-CPs}$ (R- $\text{Ni}_{10-x}\text{Fe}_x\text{-CPs}$) ($0 \leq x \leq 5$). In a typical synthetic procedure, a total of 50 mg of $\text{Ni}_{10-x}\text{Fe}_x\text{-CP}$ precursors were dispersed in 15 mL of ethanol through ultrasonication for 10 min to obtain a very homogeneous dispersion. At the same time, a total of 0.341 g (0.3 M), 1.135 g (1.0 M), and 3.405 g (3.0 M) of sodium borohydride (NaBH_4) were dissolved into 30 mL of cold DI water to obtain a transparent solution, respectively. Subsequently, the NaBH_4 solution was rapidly poured into the Ni-CP dispersion and stirred for 5 h. The obtained precipitation and solution were separated via centrifugation. ICP-MS results show that the solution contains large amounts of B and Na (Table S2). Furthermore, the precipitates were collected by centrifugation, washed with DI water and ethanol, and finally dried at $70\text{ }^\circ\text{C}$ for overnight. Elemental analysis showed that the content of C and N can be neglected in the precipitate (Table S4). Based on ICP-MS and elemental analysis results, we suggest that the synthesis of R- $\text{Ni}_{10-x}\text{Fe}_x\text{-CPs}$ proceeds as follows (eq. S1):^[1]



Synthesis of Ni hydroxide (Ni-OH) and $\text{Ni}_{10-x}\text{Fe}_x\text{-LDH}$ ($x=1$, and 2). In a representative procedure, Ni-OH was prepared based on a reported literature method with slight modifications.^[2-3] A total of 0.5 mmol of nickel(II) nitrate hexahydrate and 0.2 mmol of urea were dissolved in 14 mL of DI water and stirred for 15 min to obtain a homogeneous solution. After mixing, the solution was transferred into an 18 mL Teflon-lined stainless steel autoclave and maintained at 120 °C for 24 h. The obtained green precipitate was collected by centrifugation, washed with DI water and ethanol at least 3 times and dried at 70 °C overnight before use. The synthesis of Fe-doped Ni-OH was conducted as in the above method, expect that additional iron(III) nitrate nonahydrate was dissolved into the solution. Ni-OH samples with different degrees of Fe doping were denoted as $\text{Ni}_9\text{Fe}_1\text{-LDH}$ and $\text{Ni}_8\text{Fe}_2\text{-LDH}$ (referred to as NiFe-LDH), respectively.

Synthesis of NiFe-oxides. To prepare the NiFe-oxides, a total of 100 mg of $\text{Ni}_8\text{Fe}_2\text{-CP}$ (NiFe-CP) precursor was transferred into a muffle furnace and calcined at 350 °C in air for 2 h with a ramping rate of 2 °C min⁻¹.

Synthesis of NiFe nanoparticles via reductive method (R-NiFe-NPs). In a typical synthetic route, 0.64 mol of nickel(II) chloride and 0.16 mol of iron(II) chloride tetrahydrate were dissolved in 10 mL DI water. Afterwards, 10 mL of 1 M NaBH_4 aqueous solution was rapidly injected into the above solution and stirred for 5 h. The obtained black powders of R-NiFe-NPs were collected by centrifugation, washed with DI water and ethanol, and finally dried at 70 °C overnight before use.

Preparation of Fe-free purified KOH electrolyte. It is well known that the Ni-based catalysts are quite sensitive to Fe-impurities in the KOH electrolyte. Therefore, in this study, the Fe-free KOH electrolyte was purified according to reported procedures.^[4-6] Briefly, 2 g of high purity nickel(II) nitrate hexahydrate ($\geq 99.999\%$) was dissolved in 4 mL of DI water in an acid-cleaned 50 mL polypropylene tube. 20 mL of 1 M KOH was added into the Ni containing aqueous solution to obtain high purity $\text{Ni}(\text{OH})_2$. The precipitate was centrifuged and washed thrice with 20 mL of DI water and 2 mL of 1 M KOH. Finally, the polypropylene tube was refilled with 50 mL of 1 M KOH, dispersed for another 10 min, and kept overnight. The mixtures were centrifuged and separated, and the obtained purified Fe-free KOH was transferred into a new acid-cleaned polypropylene tube for further experimental purpose. ICP-MS results showed that <1 ppb Fe was detected in the purified KOH solution (Table S3), which was quite consistent with the previous literature results.^[4-6]

Materials characterization. Powder X-ray diffraction (PXRD) patterns were recorded on a STOE STADI P diffractometer (transmission mode, Ge monochromator) with Mo K_{α} ($\lambda = 0.7093 \text{ \AA}$) operated at a voltage of 50 kV and a current of 40 mA. The microstructures were characterized using field-emission scanning electron microscopy (FESEM-Zeiss Supra 50 VP), and transmission electron microscopy (TEM-FEI Tecnai G2 Spirit). Energy-dispersive X-ray spectroscopy (EDX) attached to the FESEM instrument was used for analyzing the composition of the samples. High-resolution TEM (HRTEM), high angle annular dark field-scanning transmission electron microscopy (HAADF-STEM), and scanning transmission electron microscopy-energy dispersive X-ray spectroscopy (STEM-EDX) elemental mapping were recorded on a FEI Titan Themis equipped with a hexapole-type aberration corrector for scanning transmission electron microscopy (CEOS DCOR) and a Super EDX system. The thickness of R-NiFe-CPs was evaluated with a Cypher (Asylum Research) atomic force microscope (AFM). Attenuated total reflectance Fourier-transform infrared (FTIR) spectra were measured on a Bruker Vertex 70 spectrometer equipped with a Platinum ATR accessory containing a diamond crystal. Raman spectra were measured using a Renishaw Raman scope or InVia Qontor (Ar^+ laser, 785 nm) using pristine powder samples on quartz glass slides. X-ray photoelectron spectroscopy (XPS) studies were performed on an ESCALAB 250XI system with Al K_{α} radiation at 250 W. Electron paramagnetic resonance (EPR) spectra were recorded on a Bruker MiniScope MS 5000 spectrometer operated at room temperature. Elemental analysis was carried out with a LECO Truespec CHNS(O)-microanalyser. Inductively coupled plasma mass spectrometry (ICP-MS) was performed on an Agilent 8800 ICP-MS. X-ray absorption near-edge structure (XANES) and extended X-ray absorption fine structure (EXAFS) experiments at the Ni and Fe K -edges were performed at the Helmholtz Zentrum Berlin (HZB) BESSY II, beamline KMC 2, Berlin, Germany. EXAFS data were processed via the ATHENA software packages. The k^3 -weighted Fourier transform (FT) for all of the EXAFS data were conducted in the k -range 2 to 10 \AA^{-1} . S_0^2 was obtained based on the fitting of Ni or Fe foil and fixed to be a constant value for the other samples. The k - and R -ranges for the fitting of all of the investigated EXAFS data were limited to 2 to 10 \AA^{-1} and 1.0 to 3.5 \AA , respectively.

Preparation of working electrodes. 5.0 mg of catalysts and 2 mg carbon black were dispersed in 1 mL of ethanol and 50 μL of 5 wt% Nafion solution after sonication for 30 min to form a homogeneous ink. 3~9 μL of the catalyst ink was loaded onto a glassy carbon rotating disk electrode (GC-RDE) with a diameter of 3 mm (loading amounts $0.2\sim0.6 \text{ mg/cm}^2$). The electrode was dried at room temperature overnight before use.

Electrocatalytic oxygen evolution reaction (OER). Electrochemical measurements were carried out at room temperature in 1 M KOH with a standard three-electrode system (Metrohm Autolab PGSTAT302N potentiostat) using a Ag/AgCl electrode (3 M KCl) as reference electrode, graphite rod as the counter electrode, and GC-RDE as the working electrode, respectively. Prior to tests, the working electrode was running for 50 scans of cyclic voltammetry (CV) at 100 mV/s to reach a stable state. The OER CV curve was collected at 5 mV/s with a rotation of 1600 rpm. All measured potentials were converted to RHE using the following equation: $E(\text{RHE}) = E + E(\text{Ag/AgCl}) + 0.059 \times \text{pH}$. All polarization curves were corrected with 90 % iR-compensation. Electrochemical impedance spectroscopy (EIS) measurements were conducted in the range of 100 m Hz to 10 K Hz with a 5 mV amplitude. Durability tests were done with chronoamperometric methods at constant overpotential.

Faradaic efficiency was calculated from the equation:^[7-8]

$$\text{Faradaic efficiency} = i_{\text{ring}} / (i_{\text{disk}} \times N) \quad (\text{eq. S2})$$

where i_{disk} and i_{ring} stand for the disk and ring currents, respectively. N represents the current collection efficiency of the RRDE and is equal to 0.2. The galvanostatic method is carried out at 1600 rpm rotation speed for the measurements.

Nernst equation is given by^[9]

$$E_p = E_0 + (0.0591/n) [\log([C_{\text{ox}}]/[C_{\text{red}}])] \quad (\text{eq. S3})$$

where E_p is the redox potential, E_0 is the formal potential, n is the number of electrons involved during the electrochemical reaction process.

Randles-Sevcik equation^[9]

$$i_p = 290,000 n^{3/2} A D^{1/2} C v^{1/2} \quad (\text{eq. S4})$$

where i_p is the redox peak current (A), A represents the surface area (cm^2) of the working electrode, the diffusion coefficient of D is given in cm^2/s , C is the bulk concentration of diffusion species (mol/cm^3), and v is the scan rate (V/s).

Laviron equation^[10-11]

$$E_p = E_0 + (RT/\alpha nF) [\ln(RT k_s / \alpha nF) - \ln v] \quad (\text{eq. S5})$$

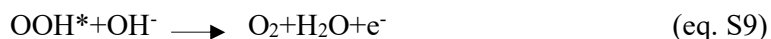
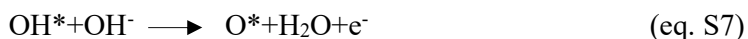
where R is the universal gas constant, T is the temperature (K), α represents the transfer coefficient, F is the Faradaic constant, and k_s is the rate constant of metal redox (s^{-1}).

Density function theory (DFT) calculations.

All DFT simulations were performed using the Vienna Ab-initio Simulation Package (VASP) with the exchange-correlation functional of generalized gradient approximation (GGA)

Perdew-Burke-Ernzerhof (PBE).^[12-13] The plane-wave cut-off energy of 500 eV was used for this study. The Brillouin zones of all systems were sampled with Gammam-point-centred Monkhorst-Pack grids. The Ni(OH)₂ (001)-terminated surface, which was determined by the HR-TEM measurements, was chosen as a computed model.^[14-15] Fe atoms were introduced afterward by substitution of partial Ni atoms, denoted as NiFe-LDH. The R-NiFe-CPs was simulated by removing some Ni and O atoms from the model, in line with the deficiencies and further results of the XAS data. A 4×4×1 supercell based on Ni(OH)₂ was used for all simulations (Table S2 and S4).^[14-15] The periodic models were fully relaxed to the ground state, and the force and energy convergence was 0.05 eV/Å and 1×10⁻⁴ eV, respectively. The DFT-D2 of Grimme was adopted to correct the Van der Waals interactions.

In the alkaline conditions, the OER involves a four-electron transfer process and can be considered as follows:^[16]



where * denotes an active adsorption site, and OH*, O*, and OOH* were the corresponding OER intermediates.

At standard conditions, the Gibbs free energies (ΔG_{M^*} , M = OH, O, and OOH) are computed from the equation $\Delta G_{M^*} = \Delta E_{M^*} + \Delta \text{ZPE} - T\Delta S$. ΔE_{M^*} represents the binding energy for the intermediates. ΔZPE and ΔS values were obtained from the computed vibrational frequencies and standard tables for the reactants and products in the gas phase. The entropy of surface adsorbed atoms/molecules was set to zero. Temperature effects were neglected in this study. Moreover, an additional bias U was introduced into each step for the computation of reaction free energy. Consequently, the above-mentioned ΔG_{M^*} was expressed by the following equation:

$$\Delta G_1 = E_{\text{OH}^*} - E^* - E_{\text{H}_2\text{O}} + 1/2 E_{\text{H}_2} + (\Delta \text{ZPE} - T\Delta S)_1 - eU \quad (\text{eq. S10})$$

$$\Delta G_2 = E_{\text{O}^*} - E_{\text{OH}^*} + 1/2 E_{\text{H}_2} + (\Delta \text{ZPE} - T\Delta S)_2 - eU \quad (\text{eq. S11})$$

$$\Delta G_3 = E_{\text{OOH}^*} - E_{\text{O}^*} - E_{\text{H}_2\text{O}} + 1/2 E_{\text{H}_2} + (\Delta \text{ZPE} - T\Delta S)_3 - eU \quad (\text{eq. S12})$$

$$\Delta G_4 = 4.92 \text{ eV} - E^* + E_{\text{OOH}^*} - E_{\text{O}_2} - 1/2 E_{\text{H}_2} - (\Delta \text{ZPE} - T\Delta S)_4 - eU \quad (\text{eq. S13})$$

Therefore, the theoretical overpotential η_{theory} is defined as:

$$\eta_{\text{theory}} = \max \{ \Delta G_1, \Delta G_2, \Delta G_3, \Delta G_4 \} / e - 1.23 \text{ V} \quad (\text{eq. S14})$$

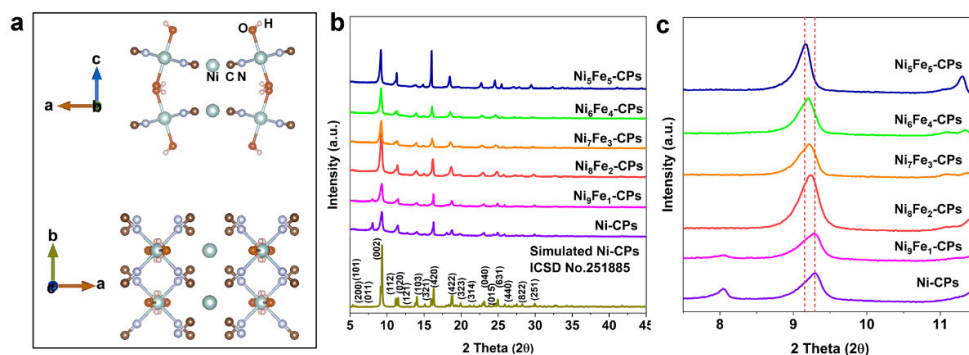


Figure S1. (a) Schematic crystal structures of Ni(H₂O)₂[Ni(CN)₄]·xH₂O (Ni-CP). (b) Simulated and experimental PXRD patterns of Ni_{10-x}Fe_x-CPs (0 ≤ x ≤ 5). (c) Peak shift to lower angles upon insertion of Fe into the Ni-CP lattice. The peaks at 2θ ≈ 8° in the Ni-CPs mainly arise from the phase with S.G. *P2/m* (ICSD No. 75541).^[17]

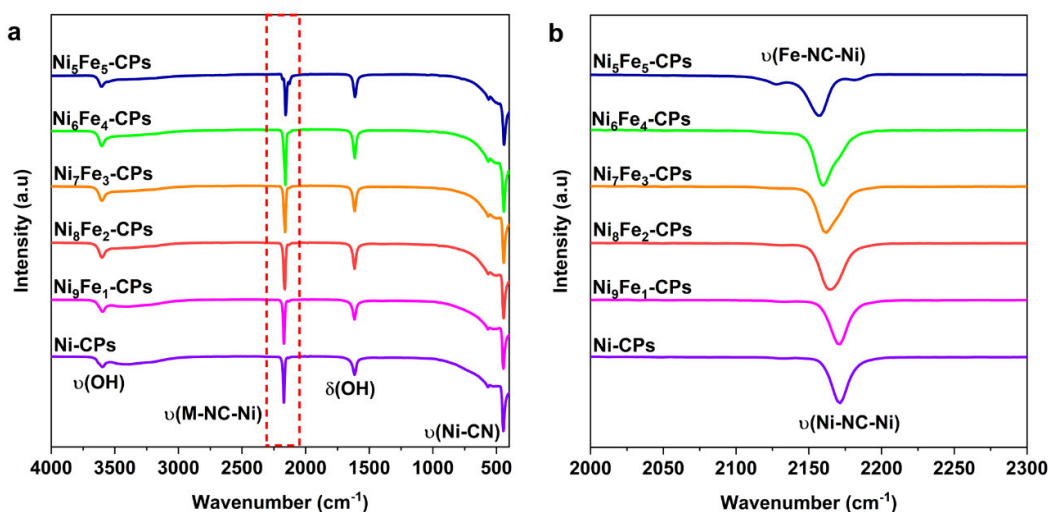


Figure S2. (a) FTIR spectra of as-prepared Ni_{10-x}Fe_x-CPs (0 ≤ x ≤ 5). (b) Zoom of the FTIR spectra in the range 2000-2300 cm⁻¹ shows a peak shift to lower wavelength upon Fe substitution.

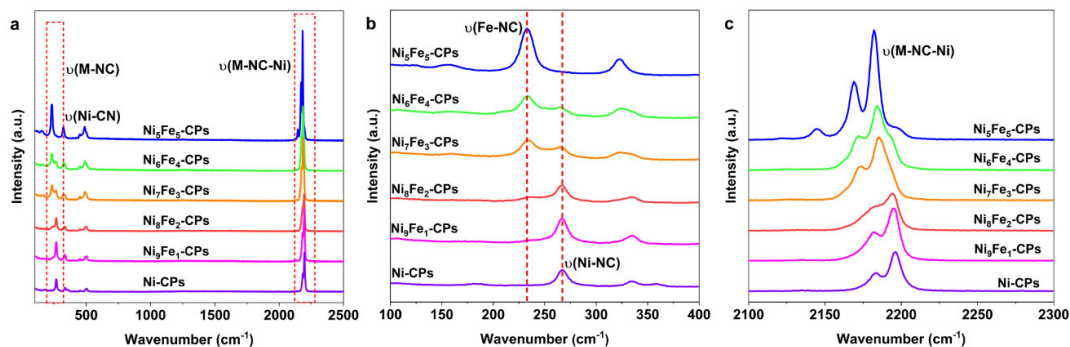


Figure S3. (a) Raman spectra of as-prepared Ni_{10-x}Fe_x-CPs (0 ≤ x ≤ 5). (b, c) Zoom of the Raman spectra in the range 100-400 cm⁻¹ and 2100-2300 cm⁻¹, respectively.

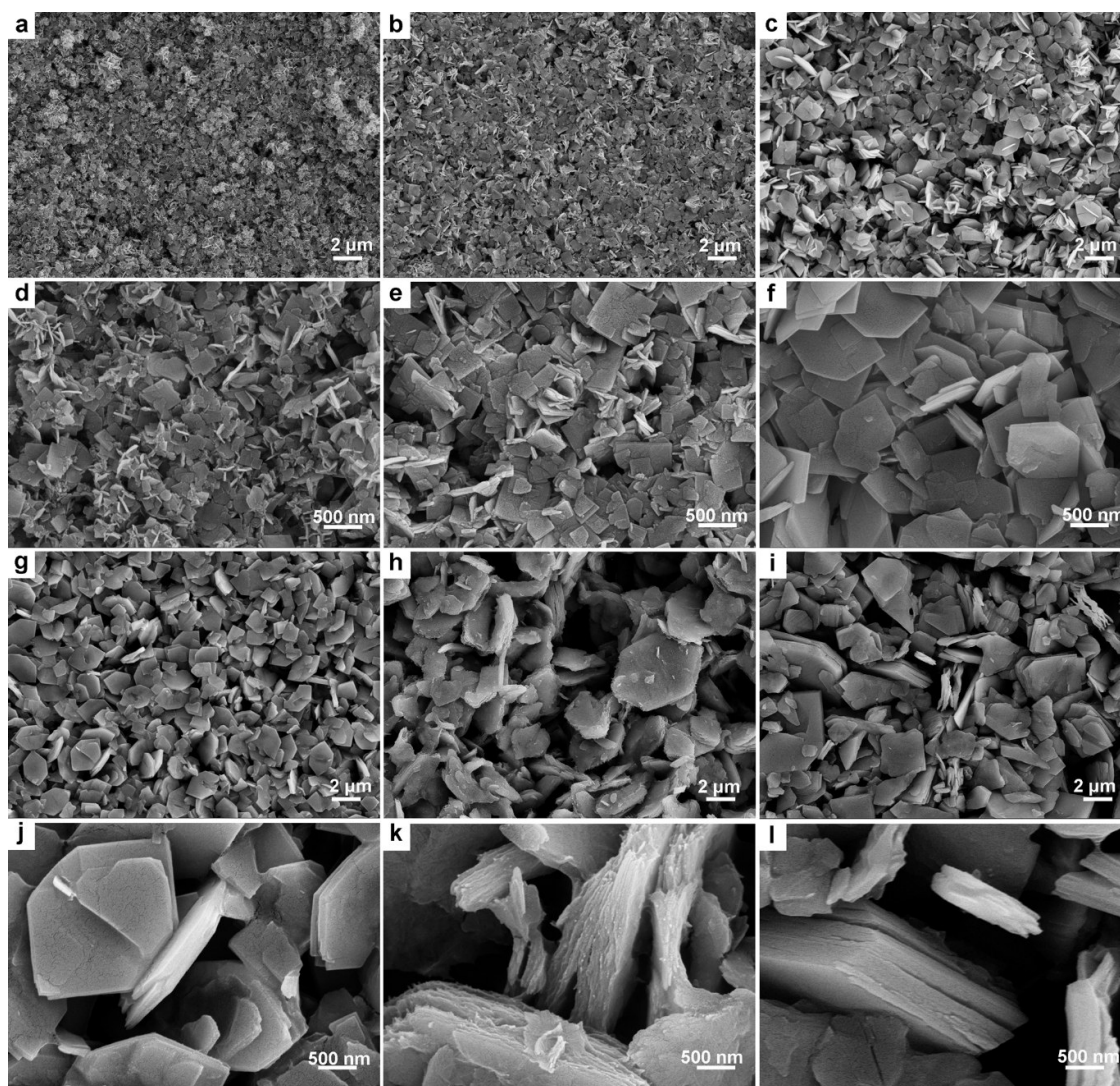


Figure S4. FESEM images of as-prepared $\text{Ni}_{10-x}\text{Fe}_x\text{-CPs}$ ($0 \leq x \leq 5$): (a, d) $x=0$; (b, e) $x=1$; (c, f) $x=2$; (g, j) $x=3$; (h, k) $x=4$; (i, l) $x=5$.

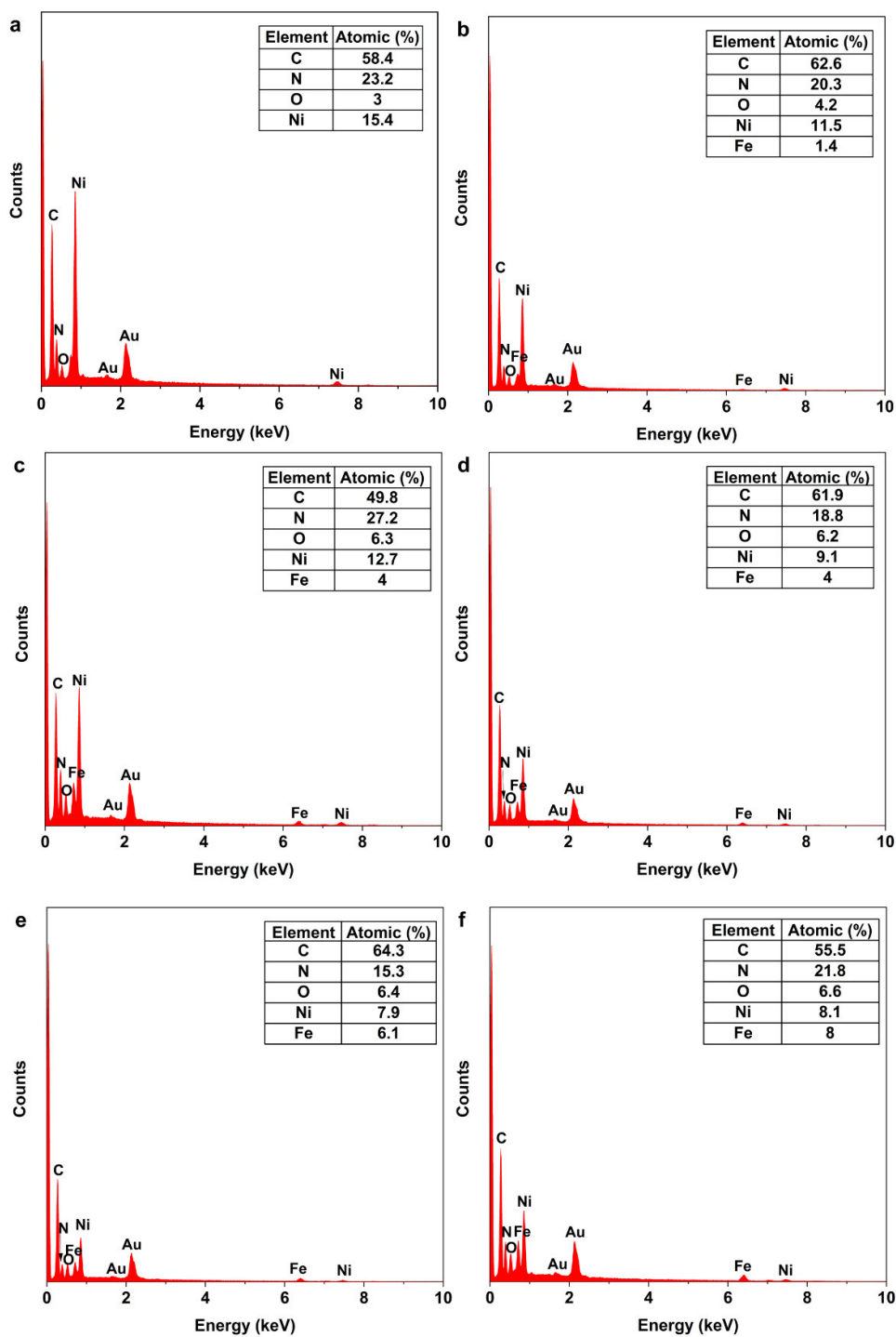


Figure S5. FESEM-EDX spectra of as-prepared $\text{Ni}_{10-x}\text{Fe}_x\text{-CPs}$ ($0 \leq x \leq 5$): (a) $x=0$; (b) $x=1$; (c) $x=2$; (d) $x=3$; (e) $x=4$; (f) $x=5$.

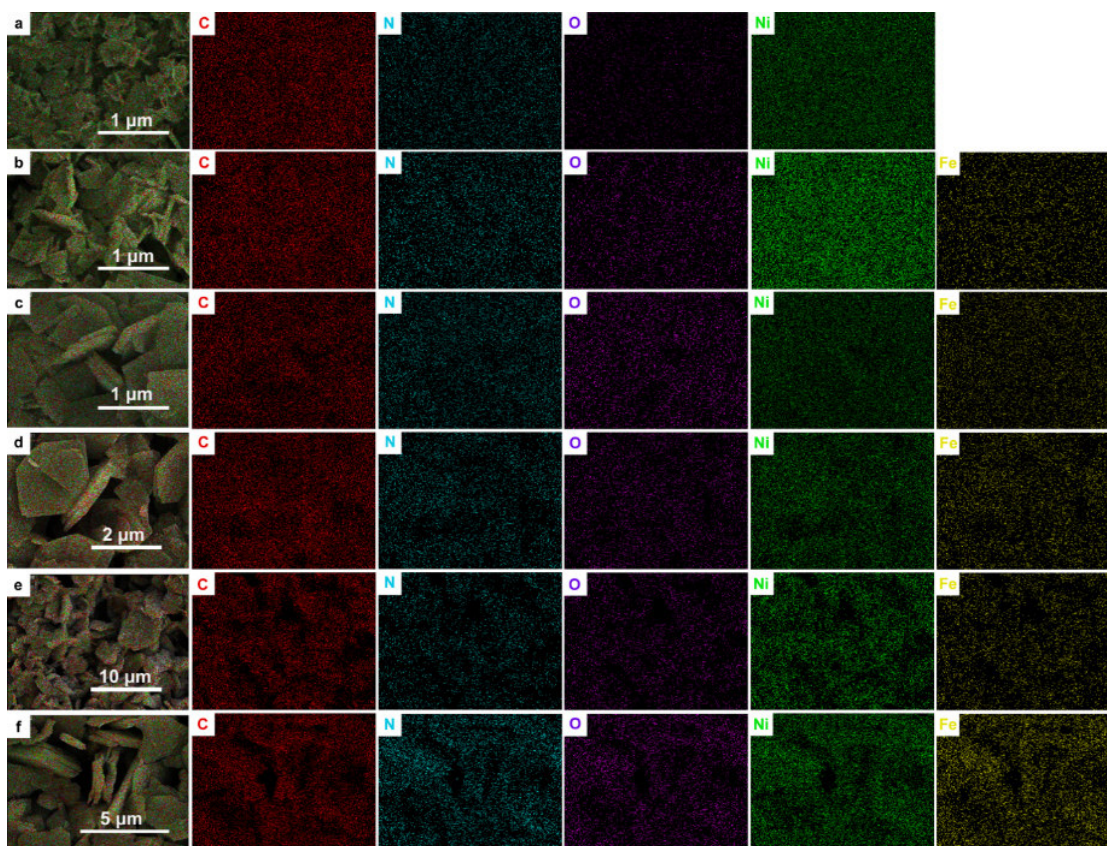


Figure S6. FESEM-EDX elemental mappings of as-prepared $\text{Ni}_{10-x}\text{Fe}_x\text{-CPs}$ ($0 \leq x \leq 5$): (a) $x=0$; (b) $x=1$; (c) $x=2$; (d) $x=3$; (e) $x=4$; (f) $x=5$.

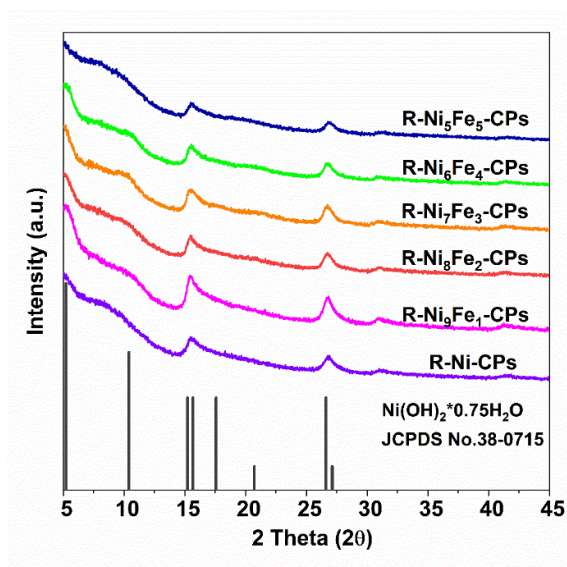


Figure S7. PXRD patterns of as-prepared $\text{R-Ni}_{10-x}\text{Fe}_x\text{-CPs}$ ($0 \leq x \leq 5$).

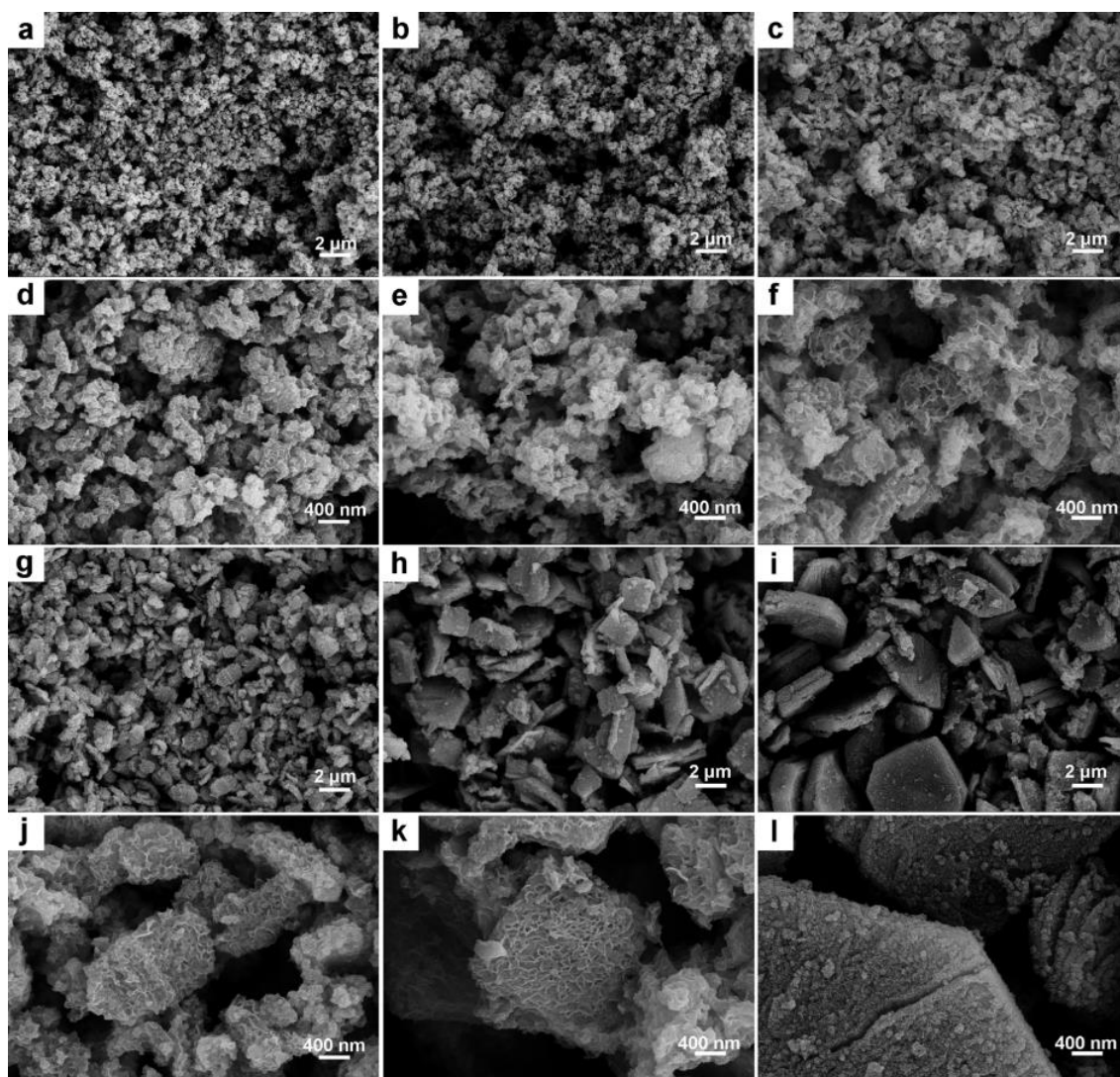


Figure S8. FESEM images of as-prepared R-Ni_{10-x}Fe_x-CPs ($0 \leq x \leq 5$): (a, d) $x=0$; (b, e) $x=1$; (c, f) $x=2$; (g, j) $x=3$; (h, k) $x=4$; (i, l) $x=5$.

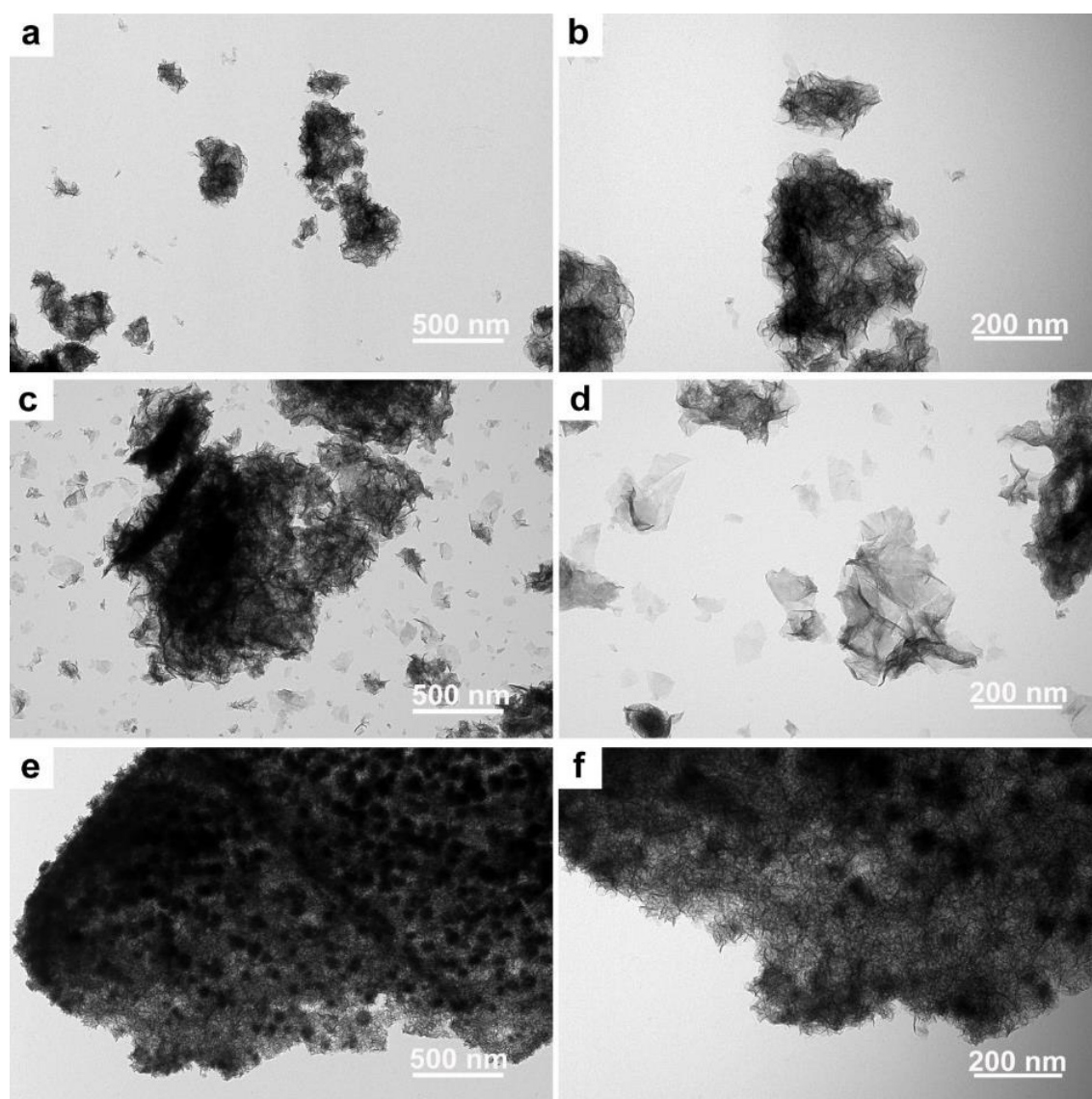


Figure S9. TEM images of as-prepared R-Ni_{10-x}Fe_x-CPs: (a, b) x=0; (c, d) x=2; (e, f) x=5.

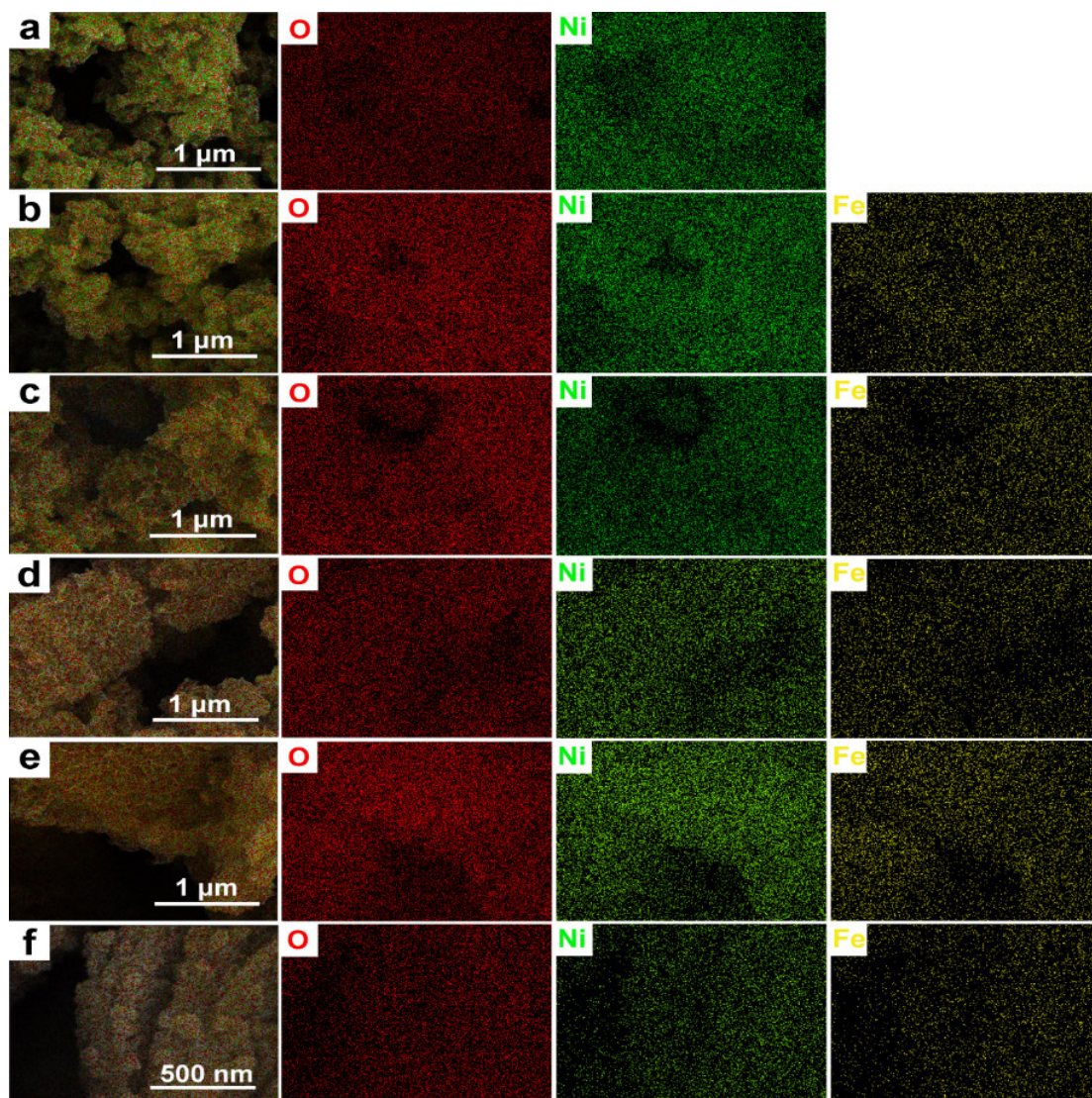


Figure S10. FESEM-EDX elemental mappings of as-prepared R-Ni_{10-x}Fe_x-CPs ($0 \leq x \leq 5$): (a) $x=0$; (b) $x=1$; (c) $x=2$; (d) $x=3$; (e) $x=4$; (f) $x=5$.

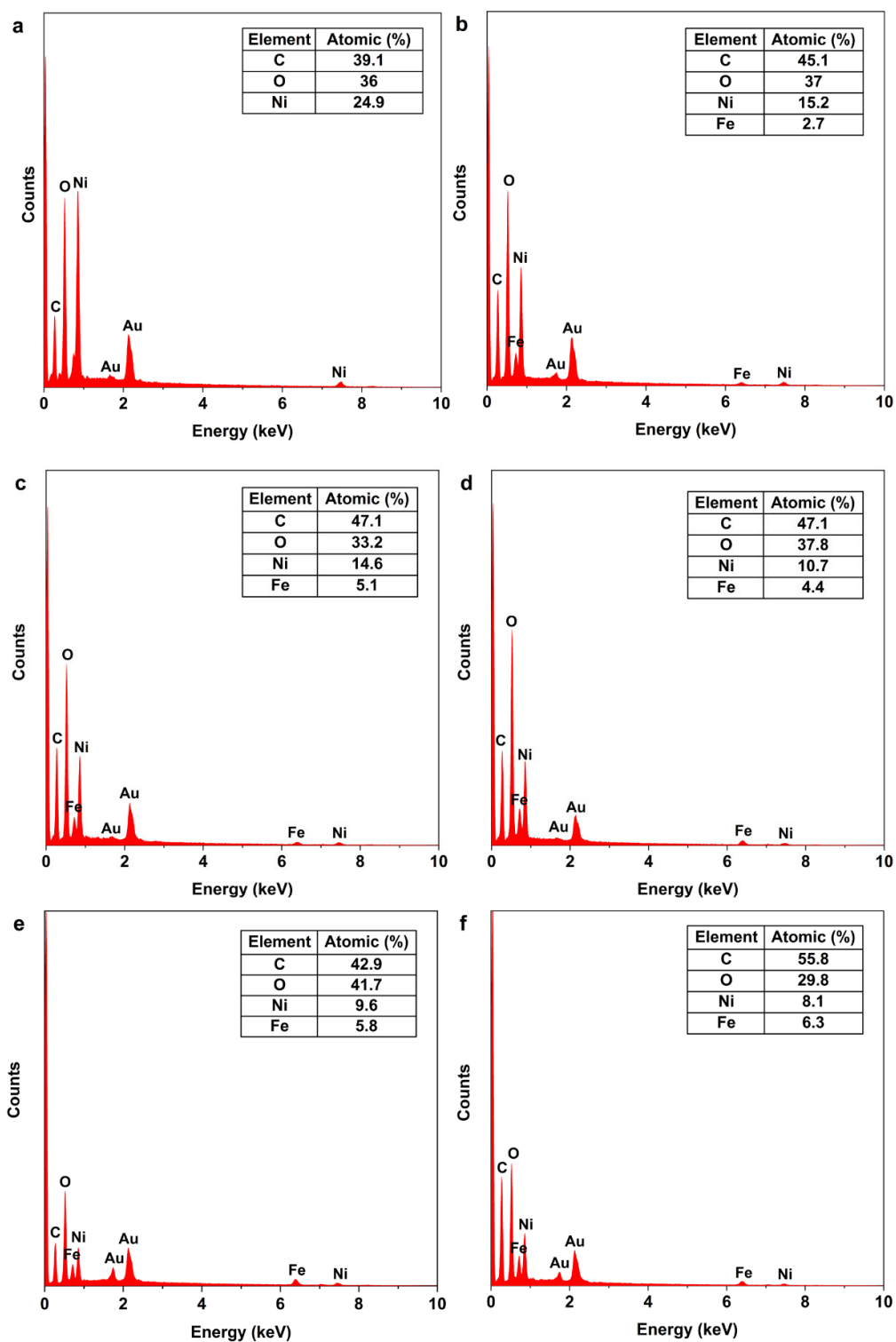


Figure S11. FESEM-EDX spectra of as-prepared R-Ni_{10-x}Fe_x-CPs ($0 \leq x \leq 5$): (a) $x=0$; (b) $x=1$; (c) $x=2$; (d) $x=3$; (e) $x=4$; (f) $x=5$.

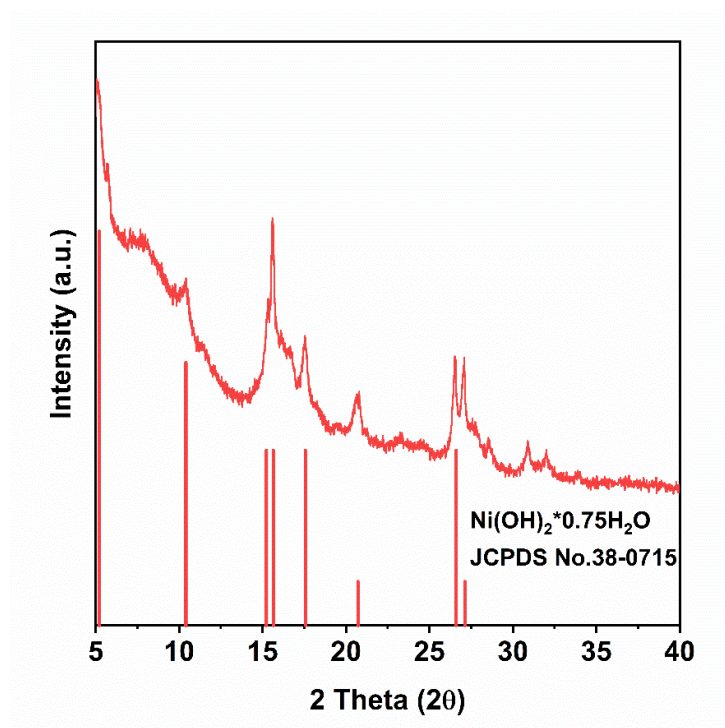


Figure S12. PXRD pattern of as-prepared NiFe-LDH (referred to as $\text{Ni}_8\text{Fe}_2\text{-LDH}$).

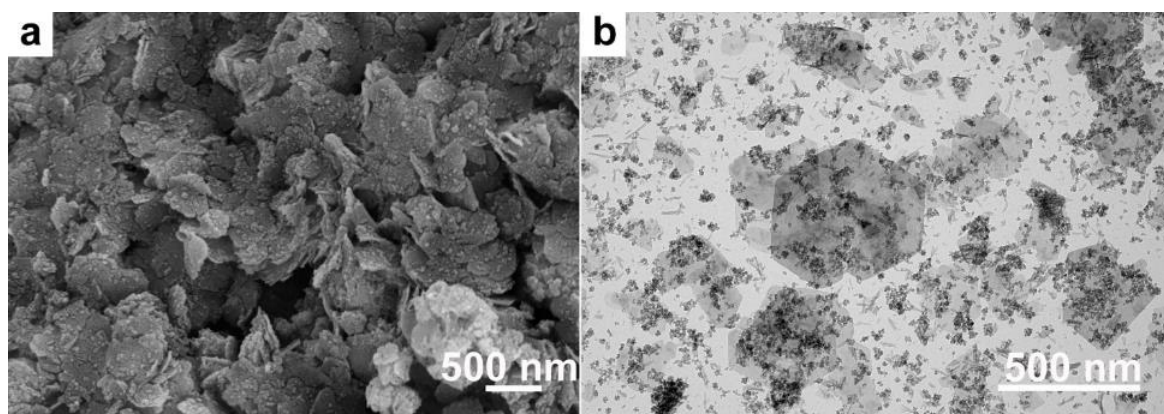


Figure S13. FESEM (a) and TEM (b) images of as-prepared NiFe-LDH.

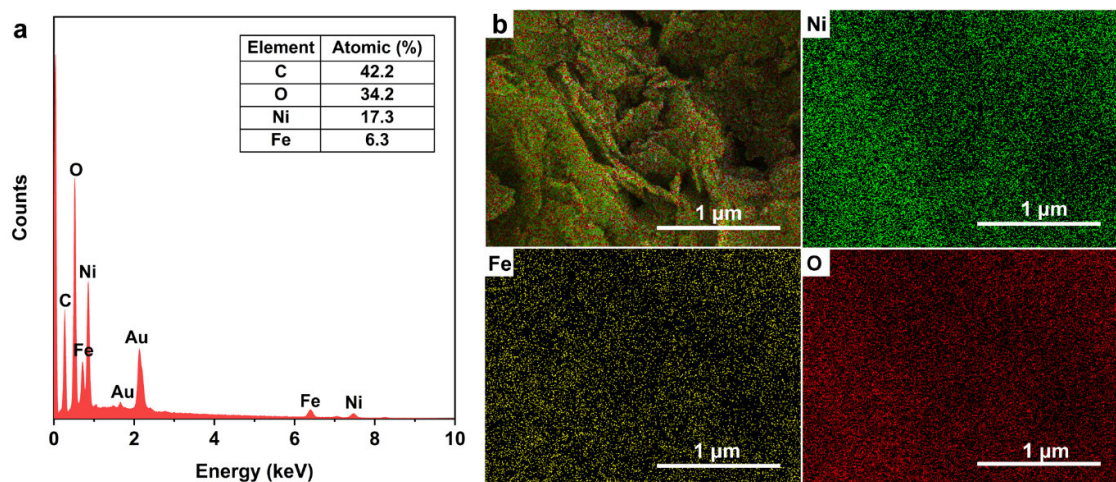


Figure S14. FESEM-EDX spectrum and elemental mappings of as-prepared NiFe-LDH.

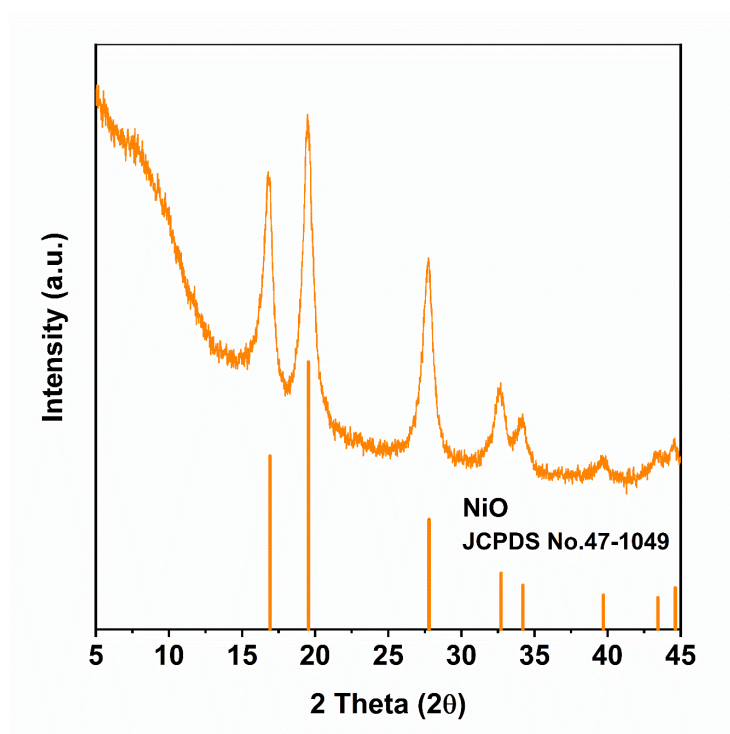


Figure S15. PXRD pattern of as-prepared NiFe-oxides.

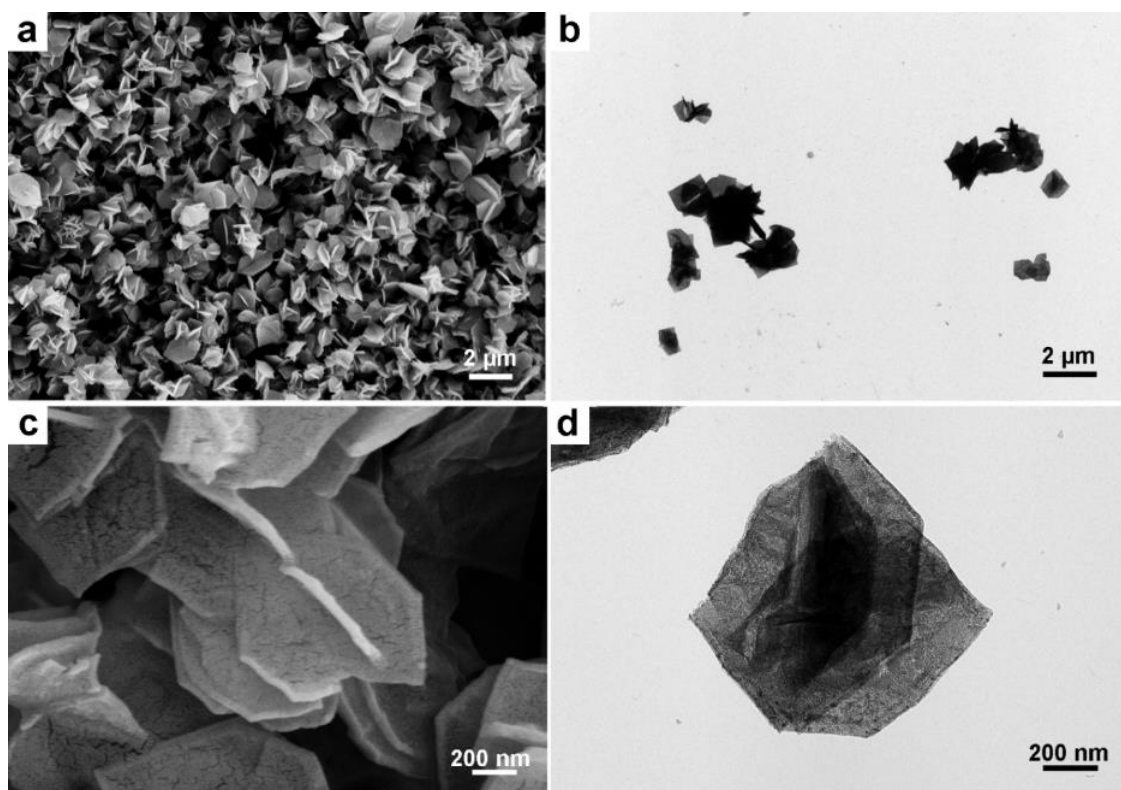


Figure S16. FESEM (a, c) and TEM (b, d) images of as-prepared NiFe-oxides.

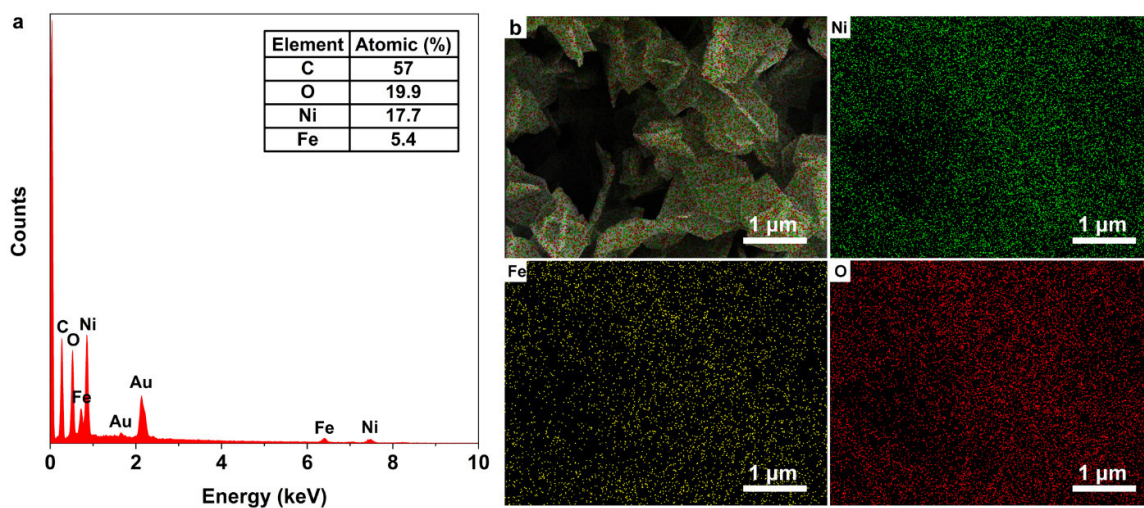


Figure S17. FESEM-EDX spectrum and elemental mappings of as-prepared NiFe-oxides.

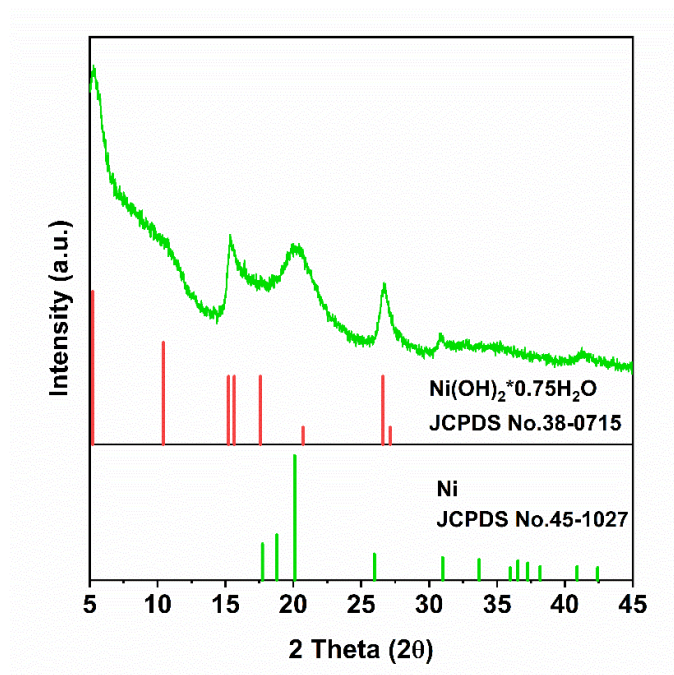


Figure S18. PXRD pattern of as-prepared R-NiFe-NPs.

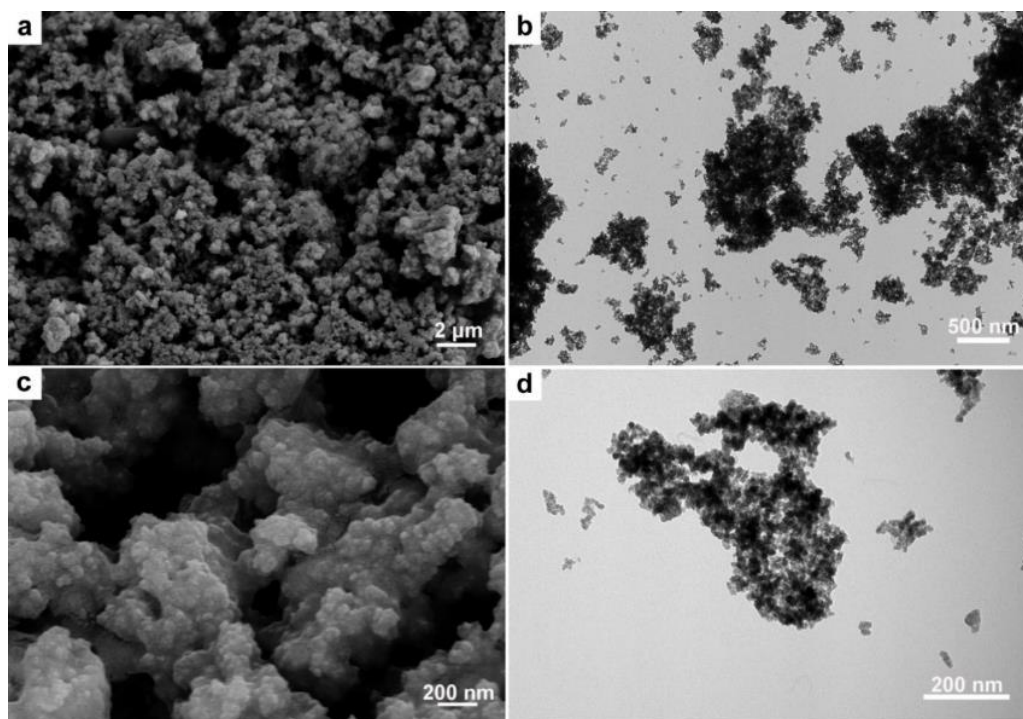


Figure S19. FESEM (a, c) and TEM (b, d) images of as-prepared R-NiFe-NPs.

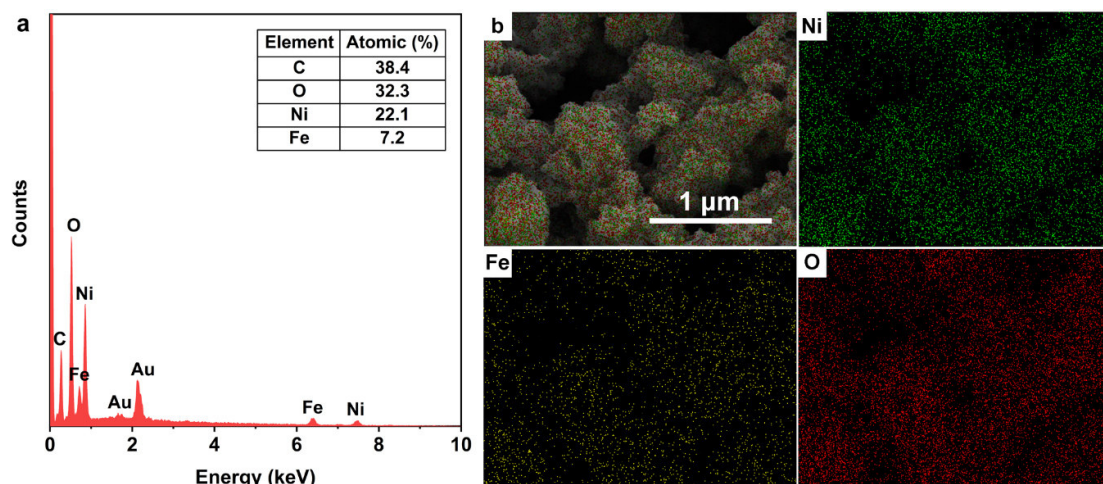


Figure S20. FESEM-EDX spectrum and elemental mappings of as-prepared R-NiFe-NPs.

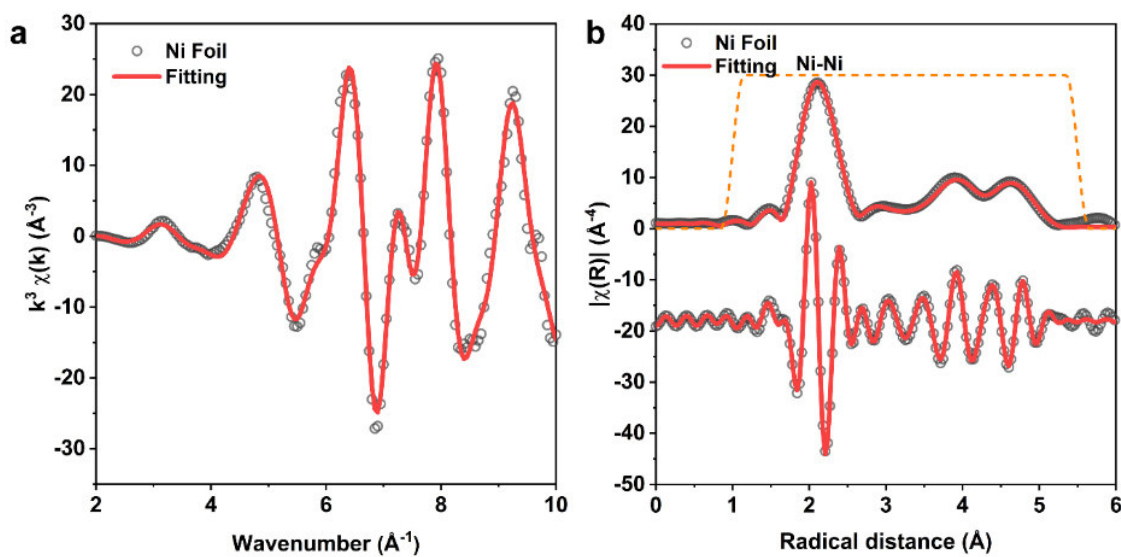


Figure S21. Fitting of the Ni *K*-edge EXAFS of reference Ni foil.

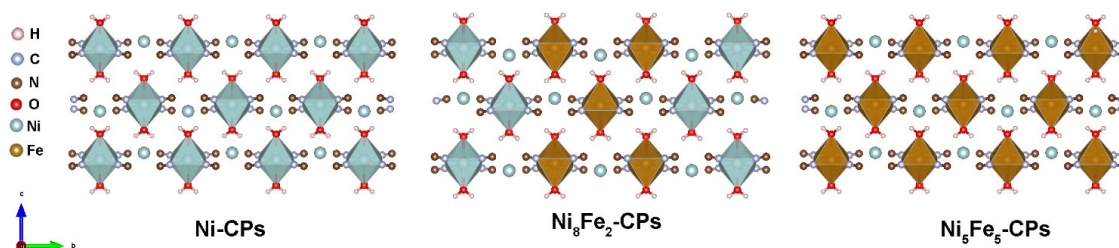


Figure S22. Schematic structure motifs of Ni-CPs, Ni₈Fe₂-CPs (referred to as NiFe-CPs), and Ni₅Fe₅-CPs.

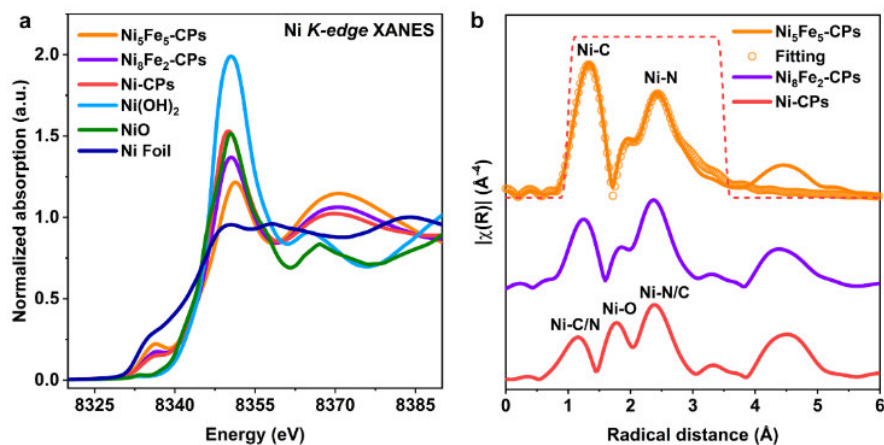


Figure S23. (a) Ni *K*-edge XANES of Ni-CPs, Ni₈Fe₂-CPs (referred to as NiFe-CPs), and Ni₅Fe₅-CPs vs. references. (b) Ni *K*-edge FT-EXAFS for the three samples (orange circles: fitting results for Ni₅Fe₅-CPs).

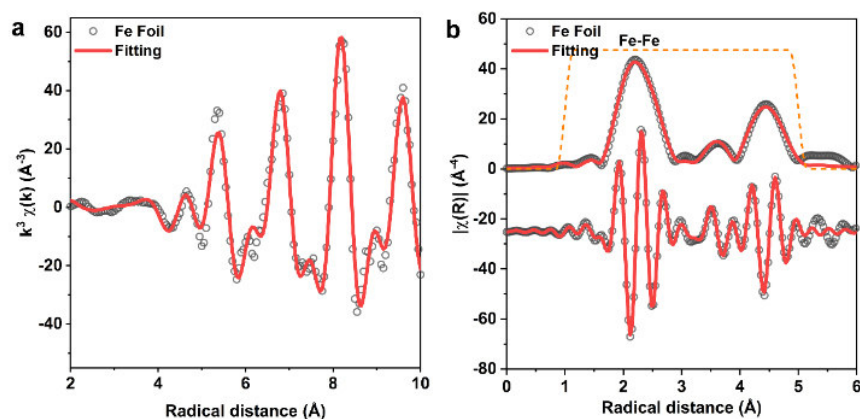


Figure S24. Fitting of the Fe *K*-edge EXAFS of reference Fe foil.

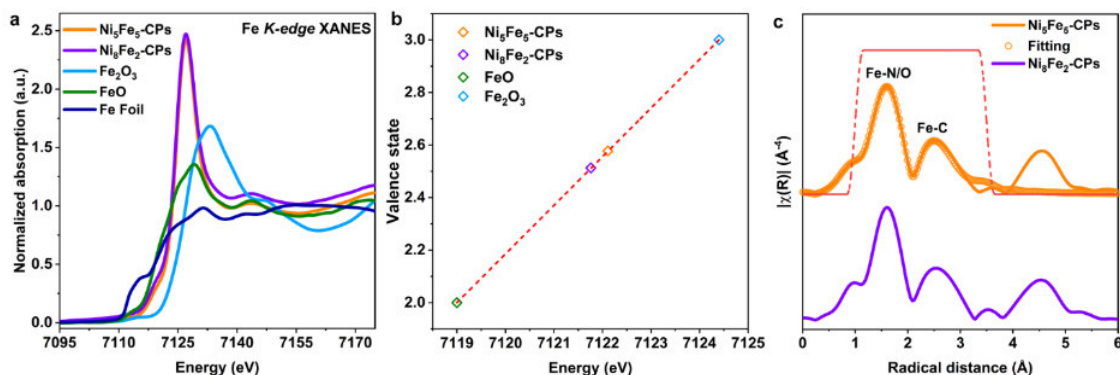


Figure S25. (a) Fe *K*-edge XANES of Ni-CPs, Ni₈Fe₂-CPs (referred to as NiFe-CPs), and Ni₅Fe₅-CPs vs. references. (b) Calculated Fe valence states. (c) Fe *K*-edge FT-EXAFS for the three samples (orange circles: fitting results of Ni₅Fe₅-CPs).

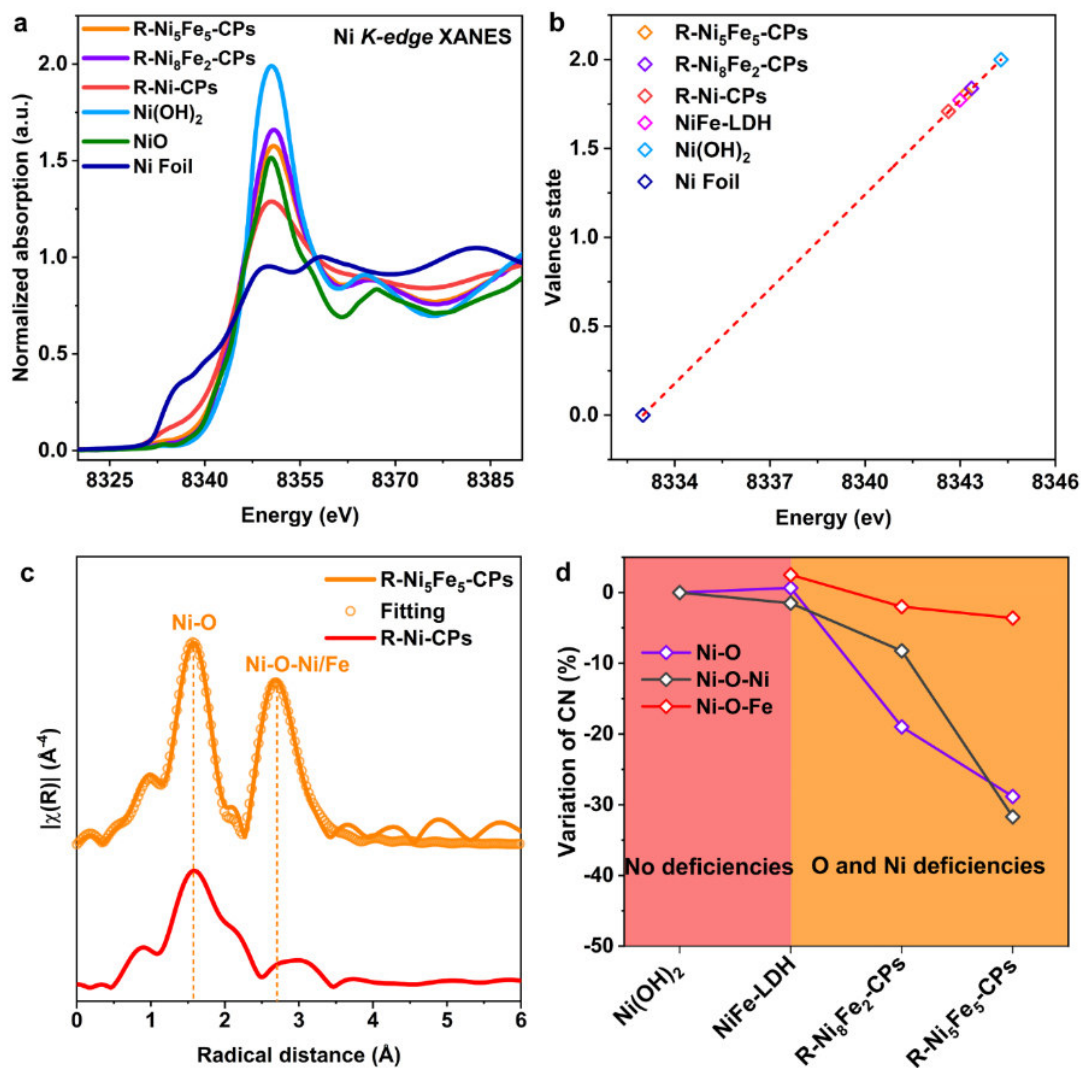


Figure S26. (a) Ni *K*-edge XANES of R-Ni-CPs, R-Ni₈Fe₂-CPs (referred to as R-NiFe-CPs), and R-Ni₅Fe₅-CPs vs. references. (b) Calculated Ni valence states. (c) Ni *K*-edge FT-EXAFS of R-Ni-CPs and R-Ni₅Fe₅-CPs (orange circles: fitting results). (d) Variation of Ni-site coordination numbers (CN).

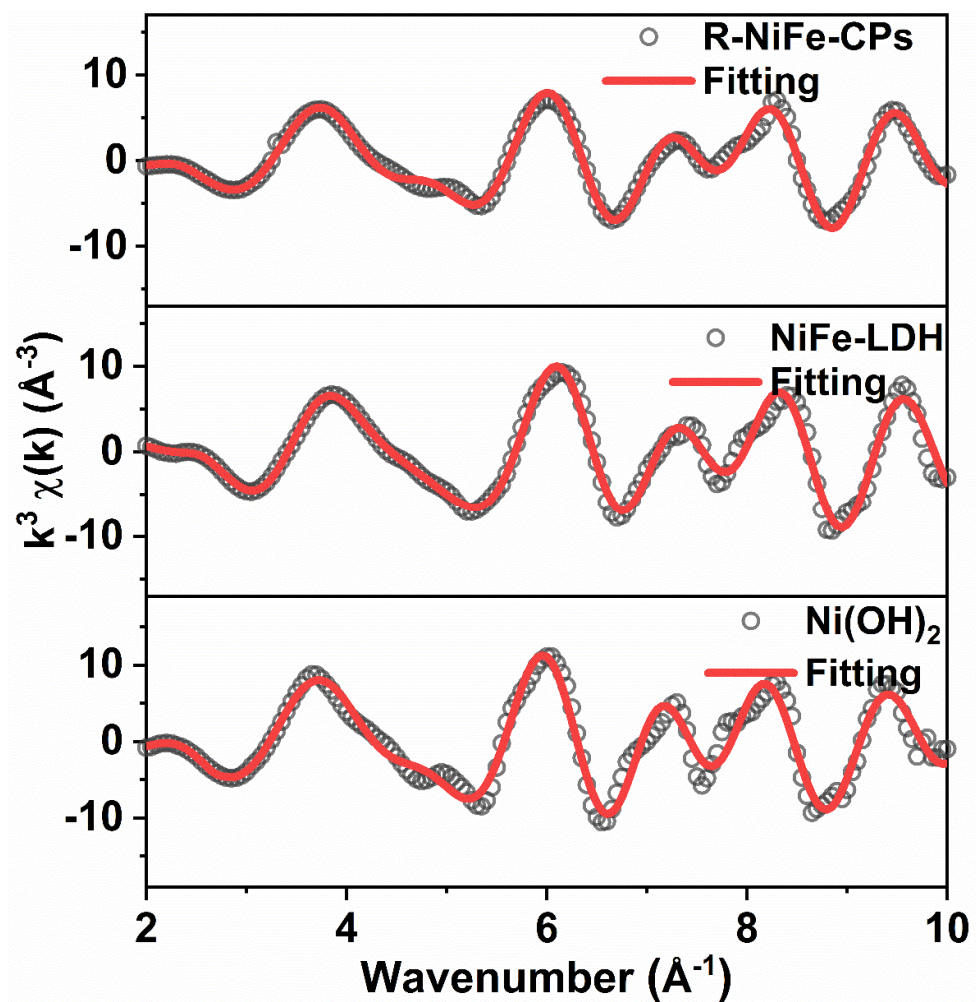


Figure S27. Fitting of the Ni *K*-edge EXAFS $k^3\chi(k)$ spectra of R-NiFe-CPs, NiFe-LDH, and reference Ni(OH)₂.

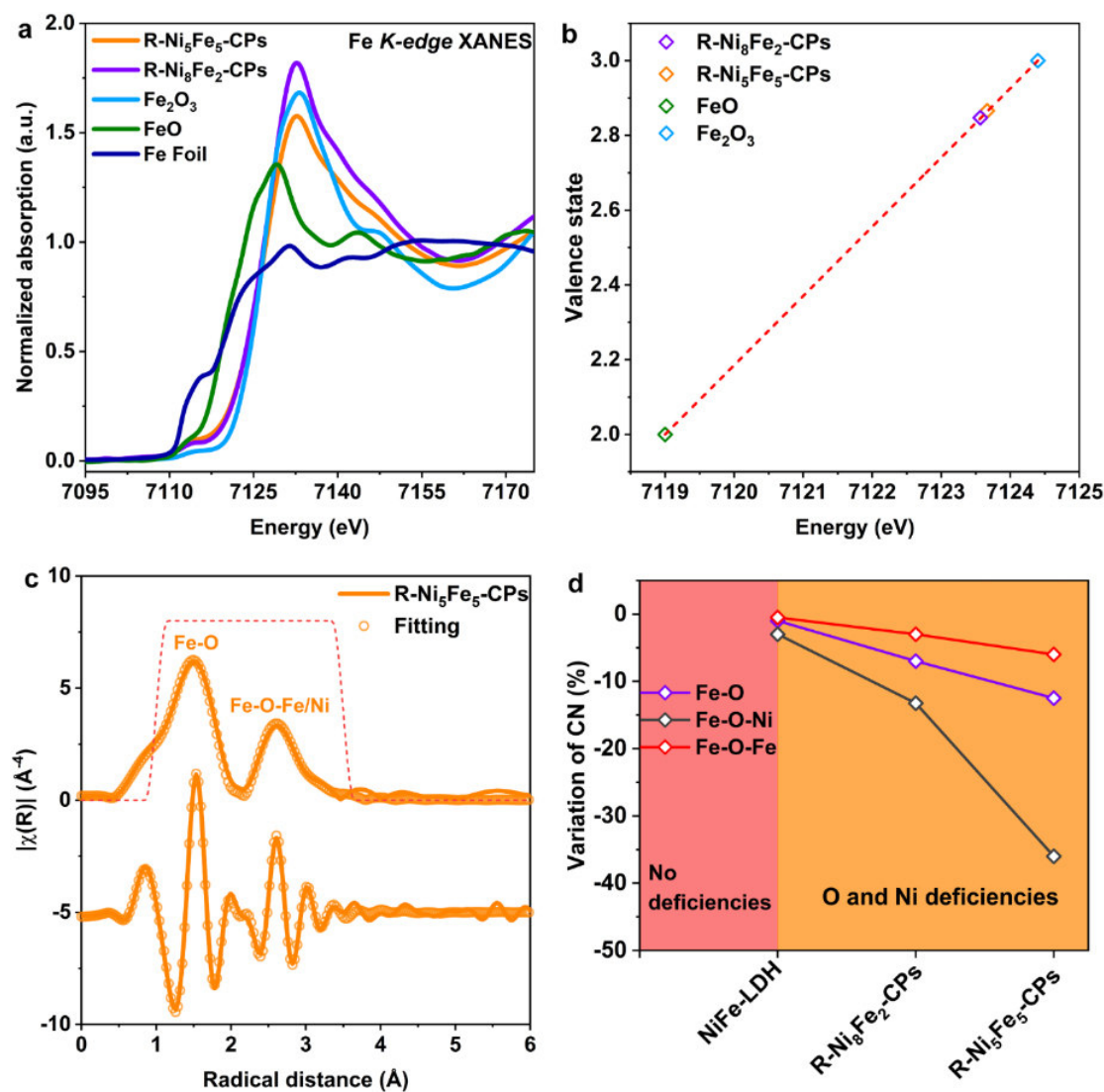


Figure S28. (a) Fe K-edge XANES of R-Ni₈Fe₂-CPs (referred to as R-NiFe-CPs) and R-Ni₅Fe₅-CPs vs. references. (b) Calculated Fe valence states. (c) Fitting of the Fe K-edge FT-EXAFS of R-NiFe₅-CPs. (d) Variation of Fe-site coordination numbers (CN) among the three samples.

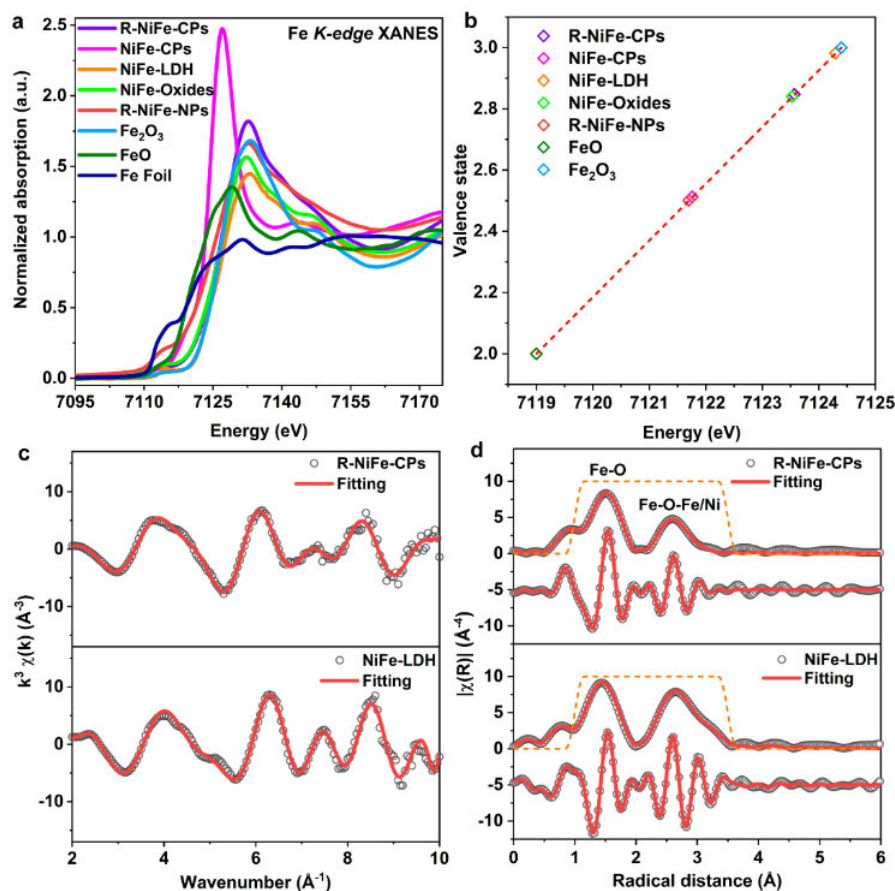


Figure S29. (a) Fe K-edge XANES of as-prepared products vs. references. (b) Calculated Fe valence states. (c, d) Fitting of the Fe K-edge EXAFS and FT-EXAFS of R-NiFe-CPs, and NiFe-LDH.

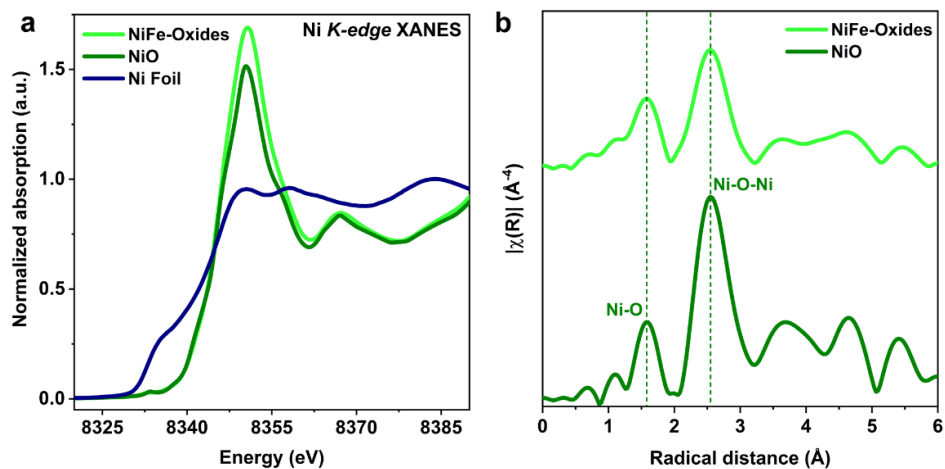


Figure S30. (a) Ni K-edge XANES of NiFe-oxides vs. references. (b) Ni K-edge FT-EXAFS of NiFe-oxides and NiO reference.

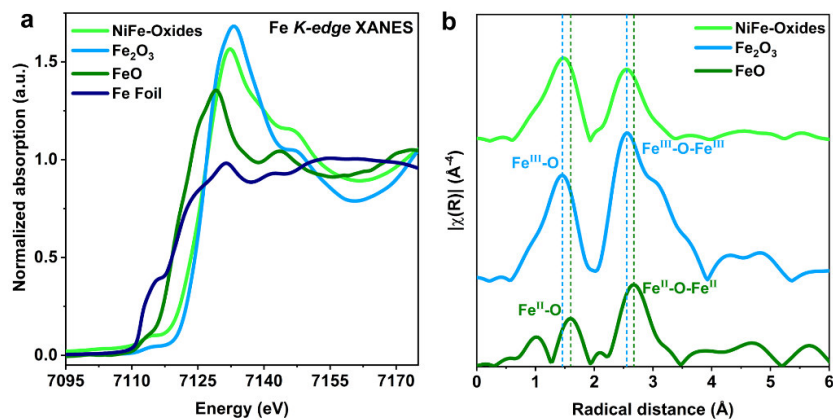


Figure S31. (a) Fe *K*-edge XANES of NiFe-oxides vs. references. (b) Fe *K*-edge FT-EXAFS of NiFe-oxides and FeO and Fe₂O₃ references.

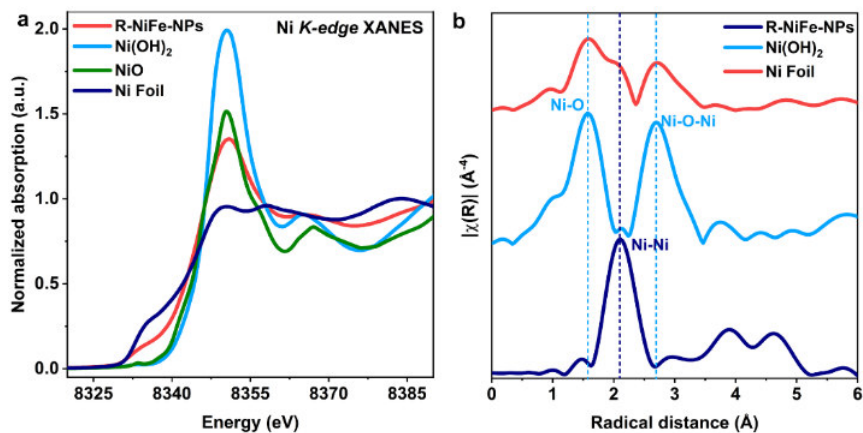


Figure S32. (a) Ni *K*-edge XANES of R-NiFe-NPs vs. references. (b) Ni *K*-edge FT-EXAFS of R-NiFe-NPs vs. references.

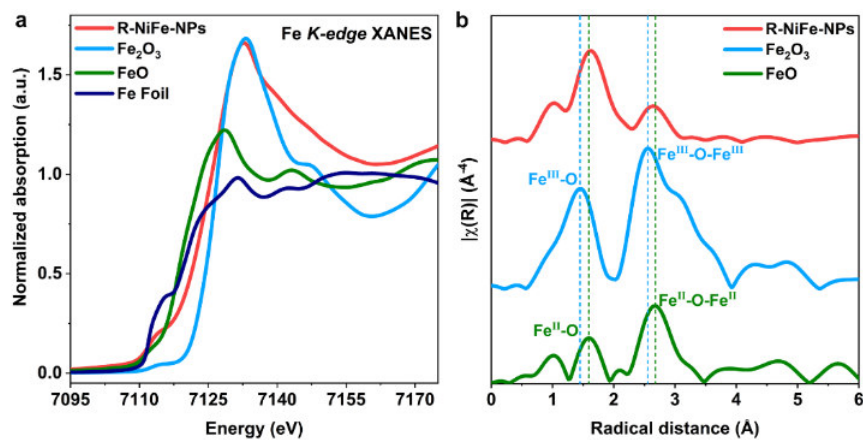


Figure S33. (a) Fe *K*-edge XANES of R-NiFe-NPs vs. references. (b) Fe *K*-edge FT-EXAFS of R-NiFe-NPs vs. references.

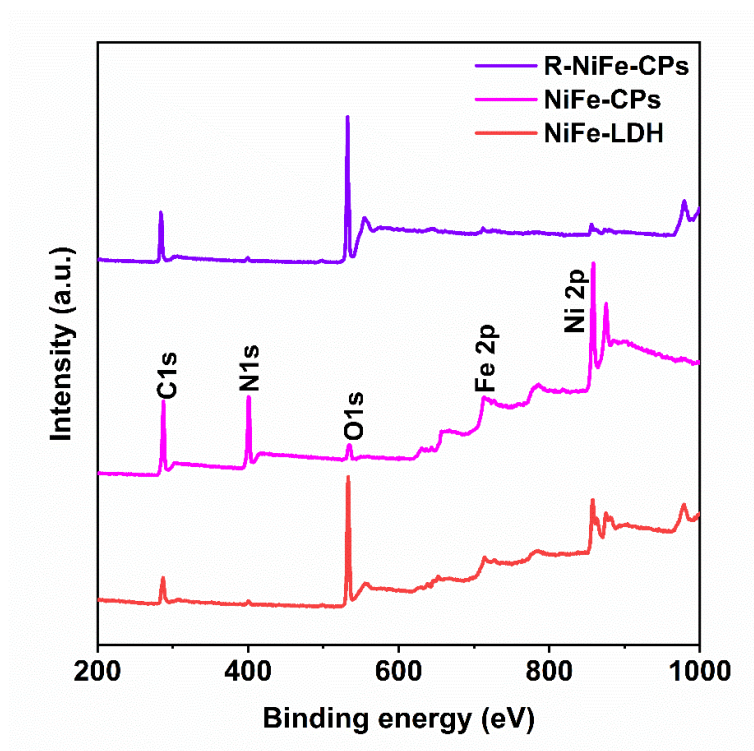


Figure S34. XPS spectra of R-NiFe-CPs, NiFe-CPs, and NiFe-LDH.

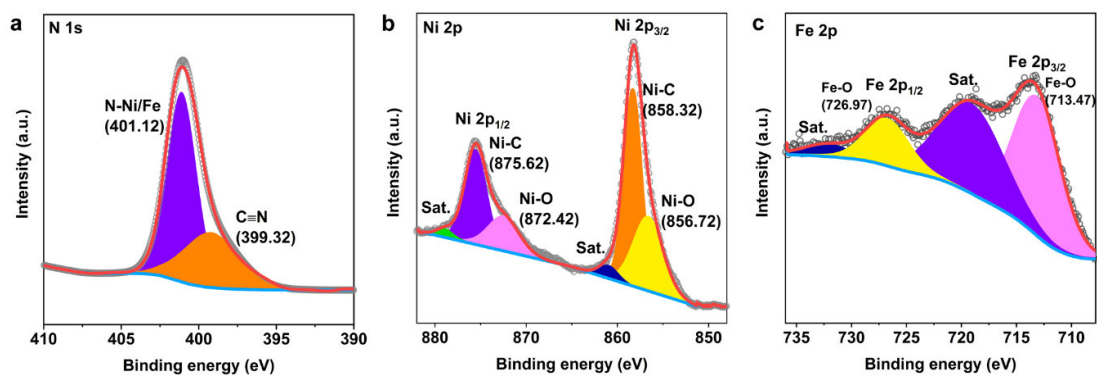


Figure S35. High-resolution XPS spectra of N 1s, Ni 2p, and Fe 2p for NiFe-CPs.

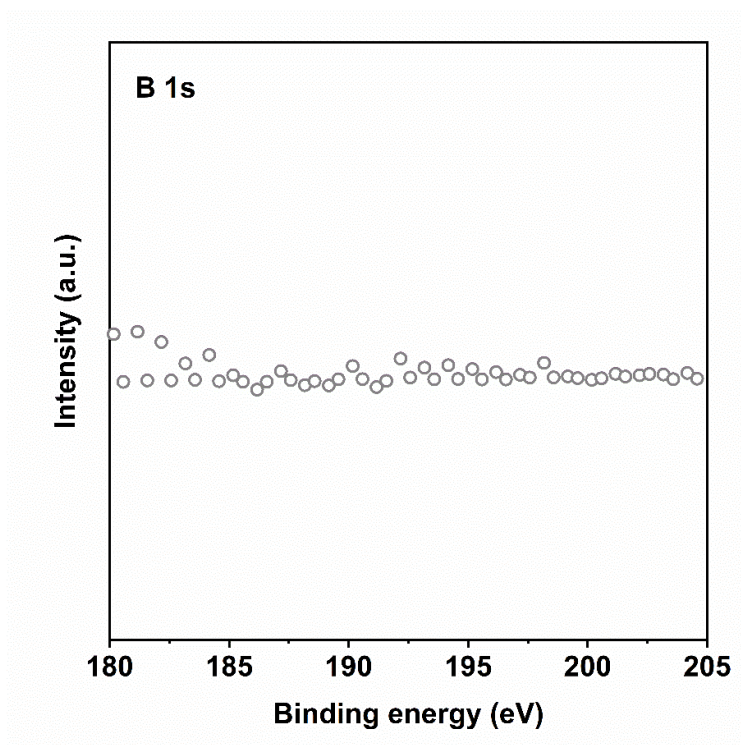


Figure S36. High-resolution XPS spectra of B 1s for R-NiFe-CPs.

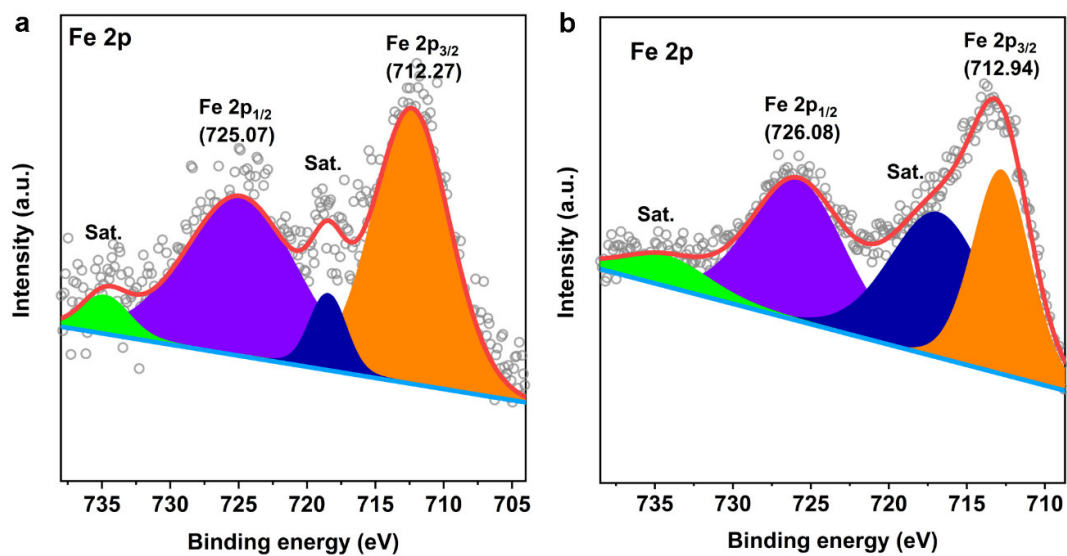


Figure S37. High-resolution XPS spectra of Fe 2p for (a) R-NiFe-CPs and (b) NiFe-LDH.

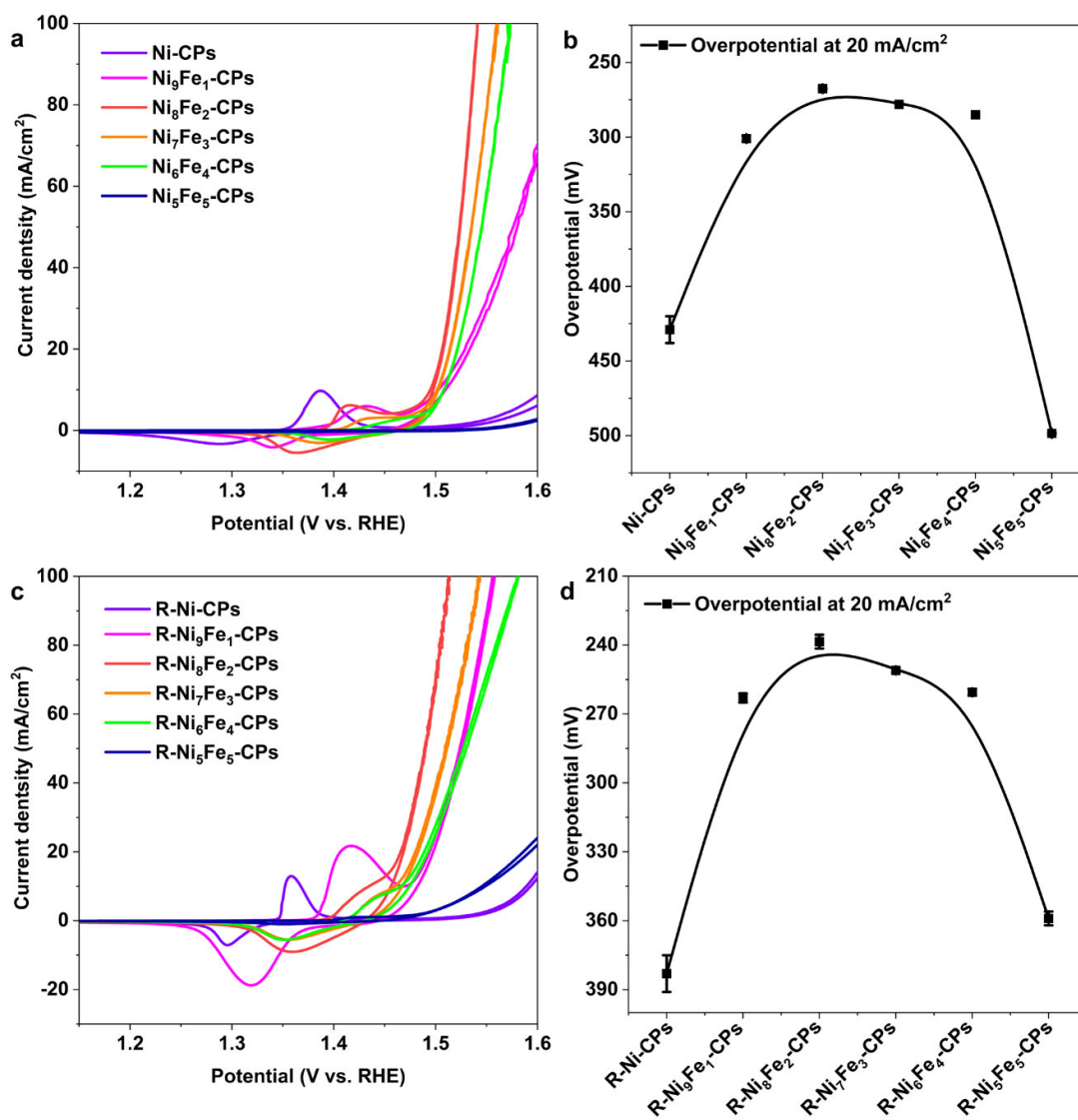


Figure S38. Electrocatalytic performance of Ni_{10-x}Fe_x-CPs and R-Ni_{10-x}Fe_x-CPs (0 ≤ x ≤ 5).

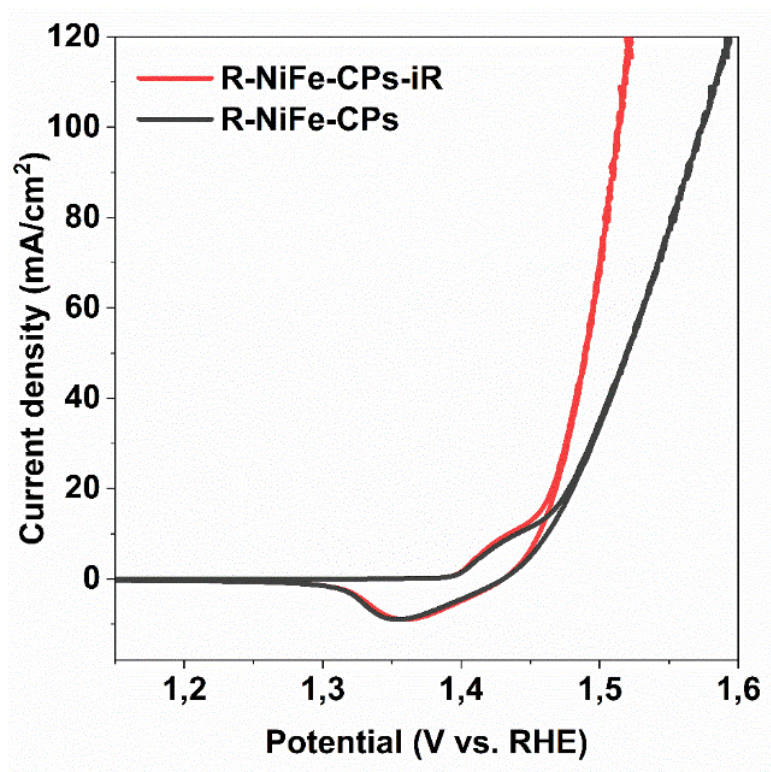


Figure S39. CV curves of R-NiFe-CPs before and after 90% iR-correction.

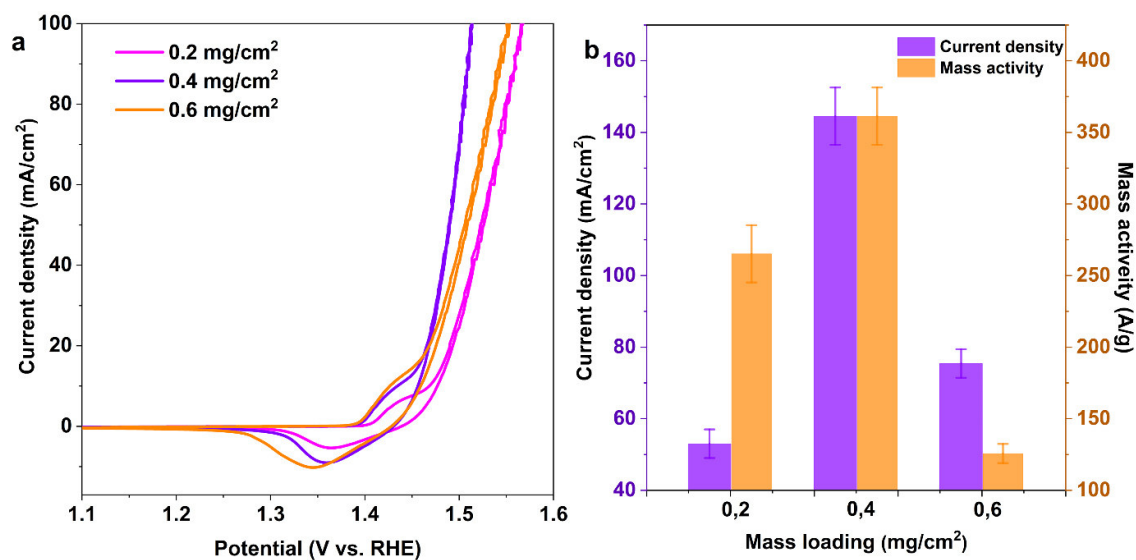


Figure S40. (a) CV curves of as-prepared R-NiFe-CPs with different mass loadings on the GC-RDE electrode. (b) Current density and mass activity of as-prepared R-NiFe-CPs at an overpotential of 300 mV.

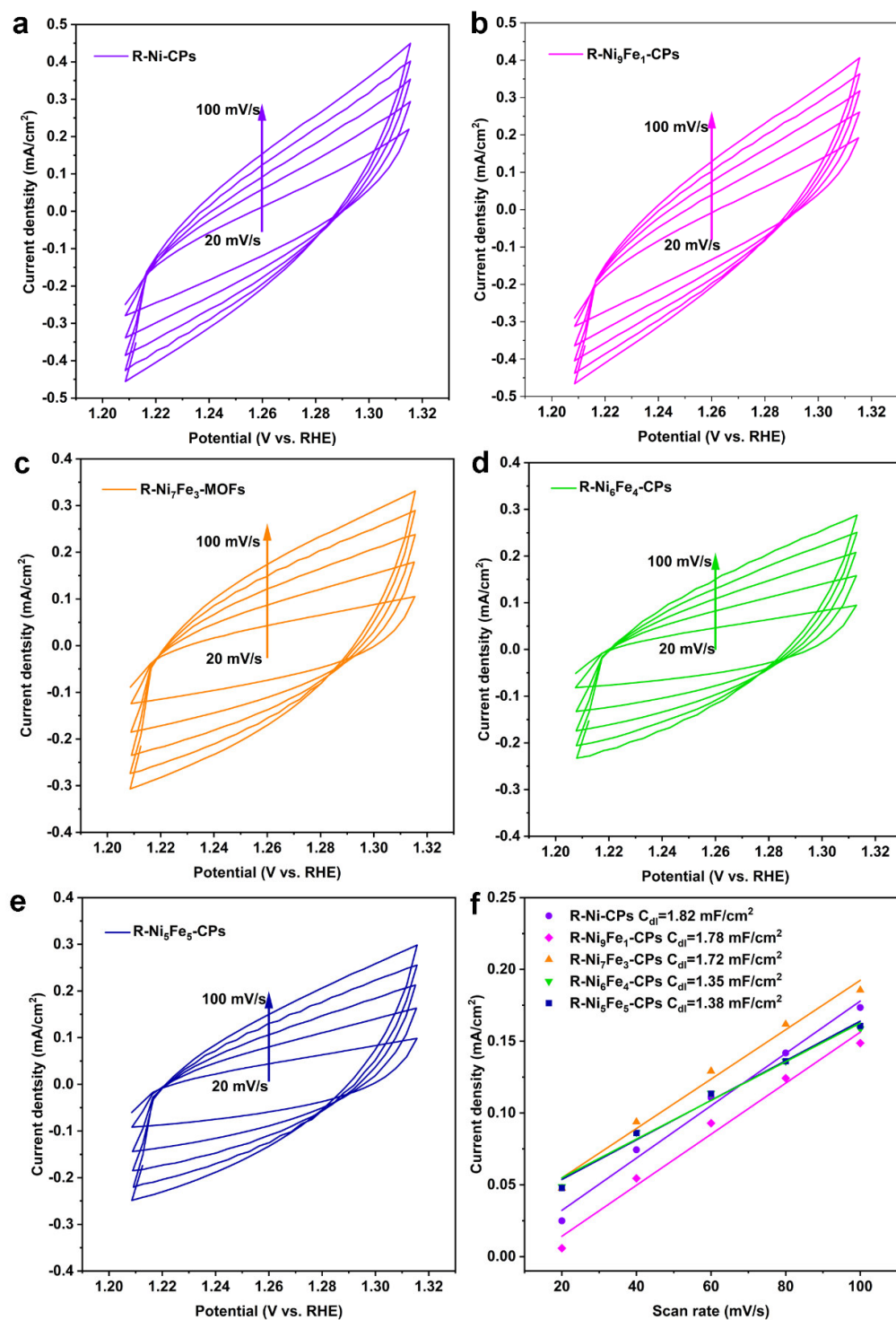


Figure S41. CV curves and double-layer capacitance (C_{dl}) of R-Ni_{10-x}Fe_x-CPs (0 ≤ x ≤ 5).

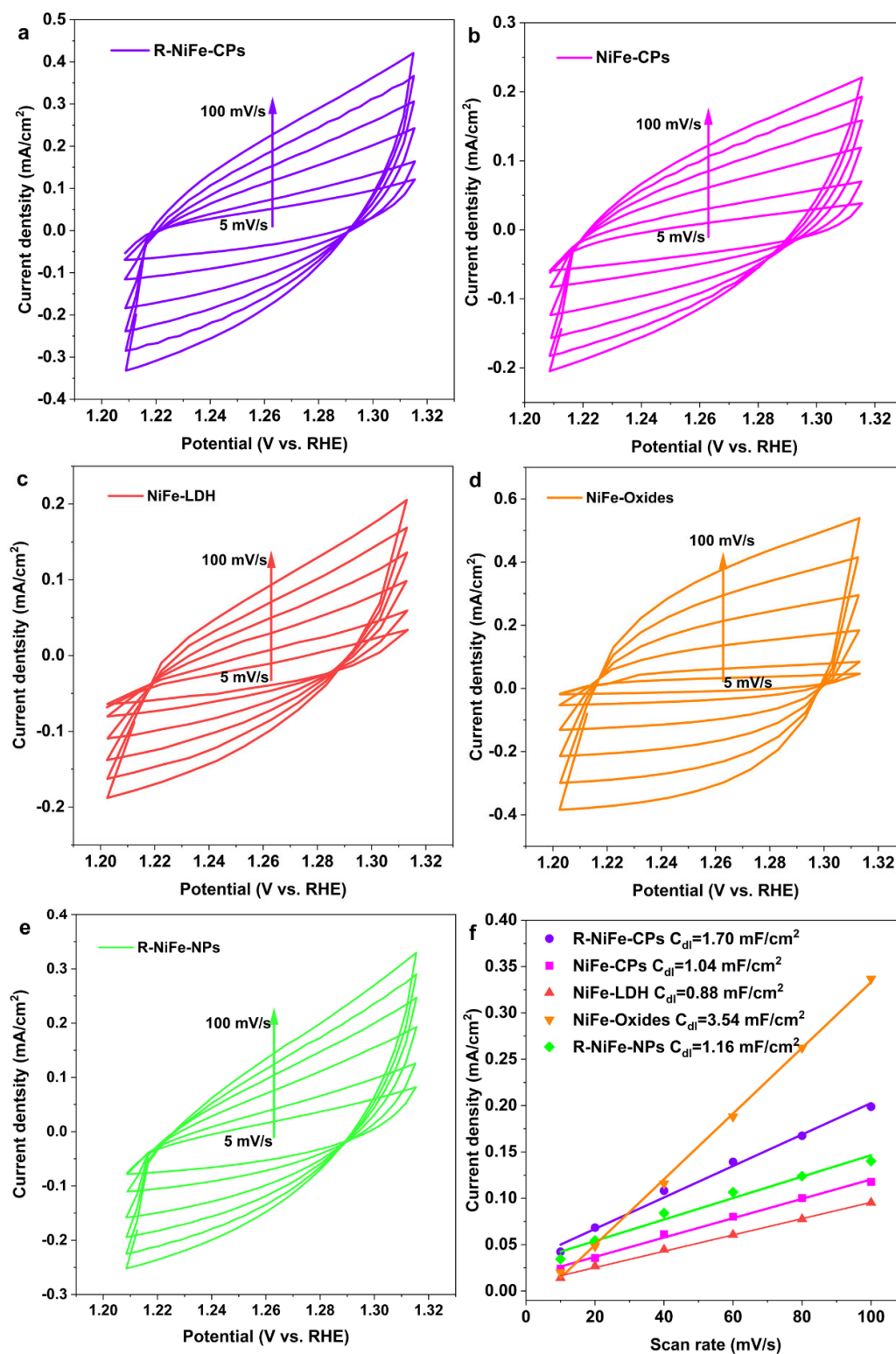


Figure S42. CV curves and double-layer capacitance (C_{dl}) of R-NiFe-CPs, NiFe-CPs, NiFe-LDH, NiFe-oxides, and R-NiFe-NPs.

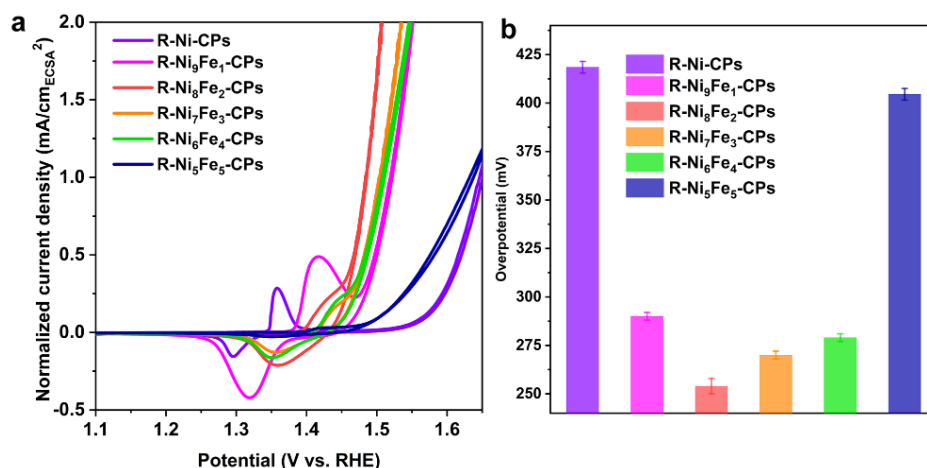


Figure S43. (a) CV curves (current normalized by ECSA) of R-Ni_{10-x}Fe_x-CPs (0 ≤ x ≤ 5). (b) Overpotential required for 1 mA/cm_{ECSA}² of the six catalysts.

To investigate the intrinsic activities of as-prepared R-Ni_{10-x}Fe_x-CPs (0 ≤ x ≤ 5), the current was normalized by the electrochemical surface area (ECSA) (**Figure S41**). The overpotentials for attaining a specific current density of 1 mA/cm_{ECSA}² (**Figure S43b**) were recorded for activity comparison. As shown in **Figure S43**, to reach a specific current density of 1 mA/cm_{ECSA}², the minimum overpotential is 254 mV for R-Ni₈Fe₂-CPs, which outperformed that of R-Ni-CPs (419 mV), R-Ni₉Fe₁-CPs (290 mV), R-Ni₇Fe₃-CPs (254 mV), R-Ni₆Fe₄-CPs (270 mV), and R-Ni₅Fe₅-CPs (404 mV). These results further demonstrate the superior intrinsic catalytic activity of as-prepared catalysts with 20% Fe substitution.

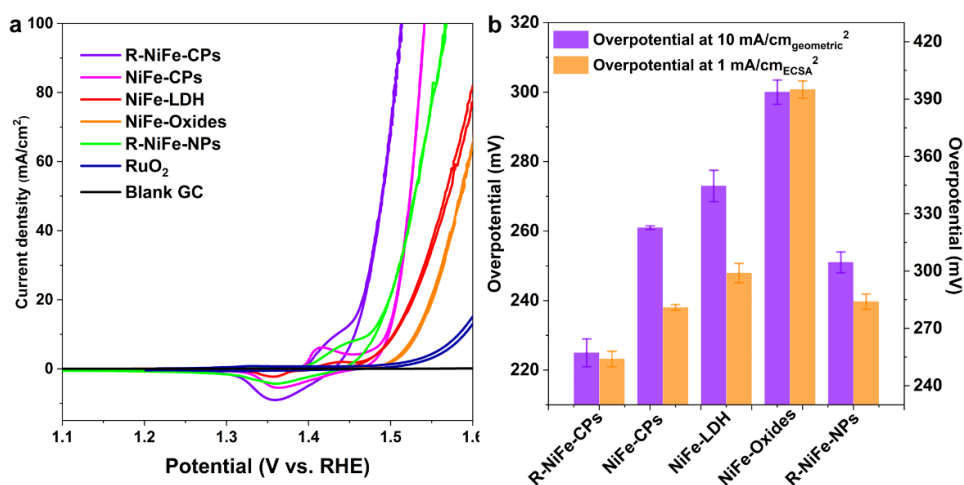


Figure S44. (a) CV curves of R-NiFe-CPs, Ni-Fe-CPs, NiFe-LDH, NiFe-oxides, and R-NiFe-NPs compared with commercial RuO₂. (b) Overpotential required for 10 mA/cm_{geometric}² and 1 mA/cm_{ECSA}² of the five catalysts.

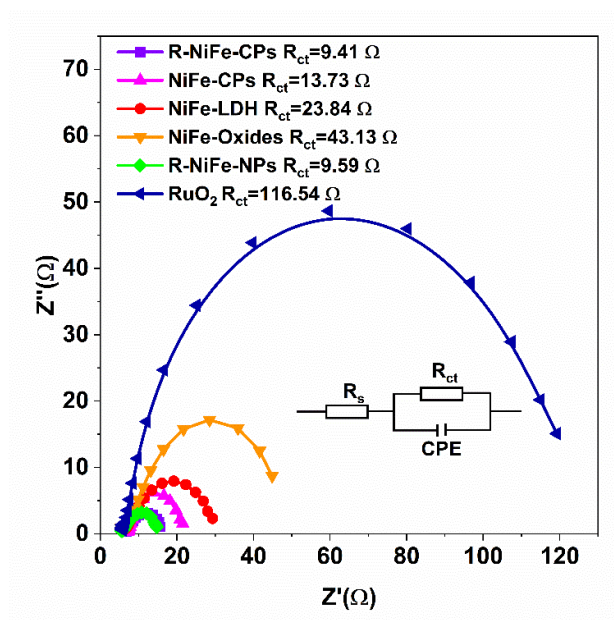


Figure S45. Nyquist plots (at an overpotential of 250 mV) of R-NiFe-CPs, Ni-Fe-CPs, NiFe-LDH, NiFe-oxides, and R-NiFe-NPs compared with commercial RuO₂.

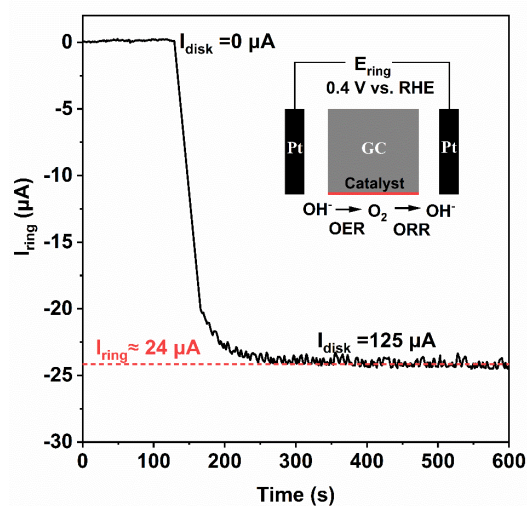


Figure S46. Faradaic efficiency measurements of R-NiFe-CPs in Ar-saturated 1 M KOH based on the RRDE technique.

To demonstrate that the observed currents arose from water oxidation rather than from other side reactions, the Faradaic efficiency was examined with the rotating ring-disk electrode (RRDE) technique. A ring current of about 24 μA was detected under the applied disk current of 125 μA (Figure S46), which corresponds to a Faradaic efficiency of 96% (eq. S2), confirming that the observed catalytic current densities were indeed arising from the OER.

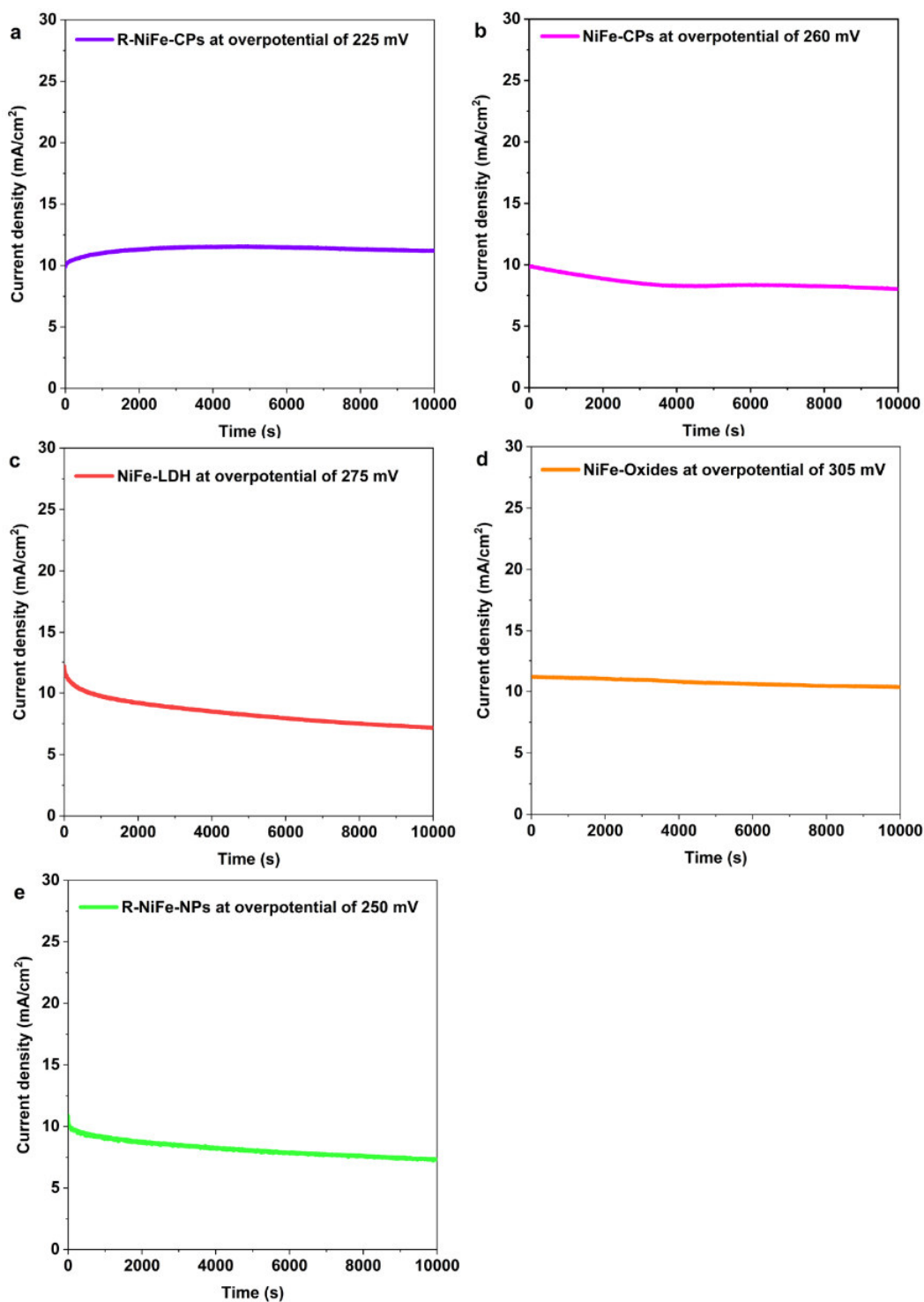


Figure S47. Chronoamperometric measurements with an applied constant overpotential for: (a) R-NiFe-CPs (at 225 mV); (b) NiFe-CPs (at 260 mV); (c) NiFe-LDH (at 275 mV); (d) NiFe-Oxides (at 305 mV); (e) R-NiFe-NPs (at 250 mV).

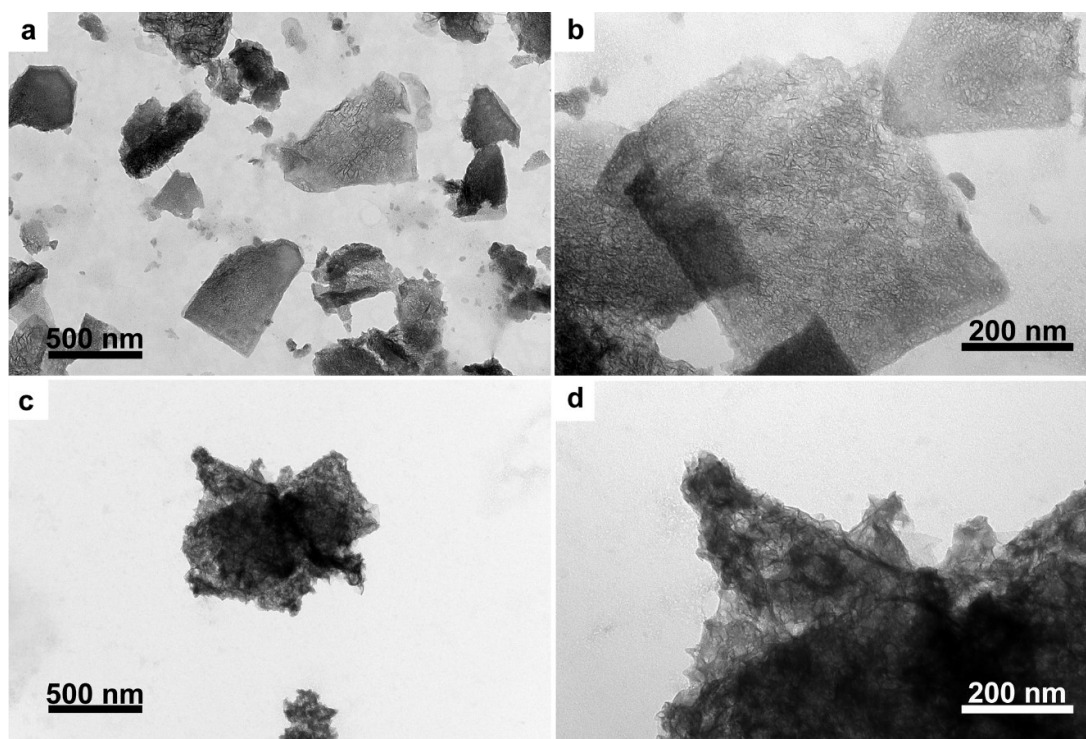


Figure S48. TEM images of NiFe-CPs (a, b) and R-NiFe-CPs (c, d) after long time measurements.

TEM images (**Figures S48a and S48b**) of post-catalytic NiFe-CPs demonstrate that the original 2D nanosheet morphologies are still maintained (**Figures 1a, e**). However, some nanoclusters were found on the surface of nanosheet substrate for the post-catalytic NiFe-CPs (**Figure S48b**). The formation of smaller nanoclusters is associated with the structural instability of NiFe-CPs during the OER process.^[47] Under alkaline conditions, the NiFe-CPs convert in situ into NiFe-based oxide/hydroxides, in line with previous studies.^[47] Post-catalytic morphological characterizations of the R-NiFe-CPs confirmed that the nanosheet structures retained their initial morphology as illustrated by TEM images (**Figures S48c, S48d**). These results demonstrate the superior stability of the as-prepared R-NiFe-CPs, which renders them very promising for the low-cost and noble metal-free OER electrocatalysts.

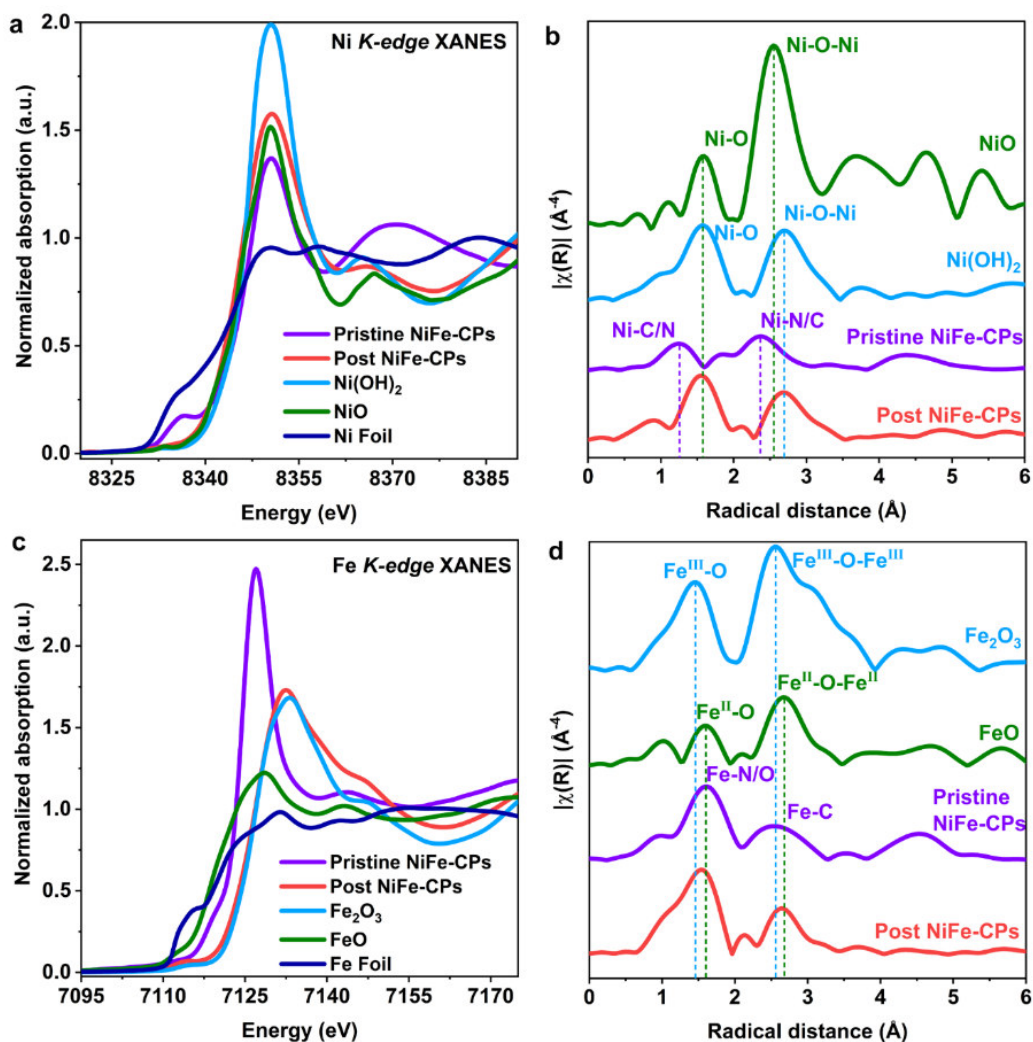


Figure S49. (a, b) Ni K-edge XANES and the corresponding FT-EXAFS spectra of NiFe-CPs before and after OER measurements vs. references. (c, d) Fe K-edge XANES and the corresponding FT-EXAFS spectra of NiFe-CPs before and after OER measurements vs. references.

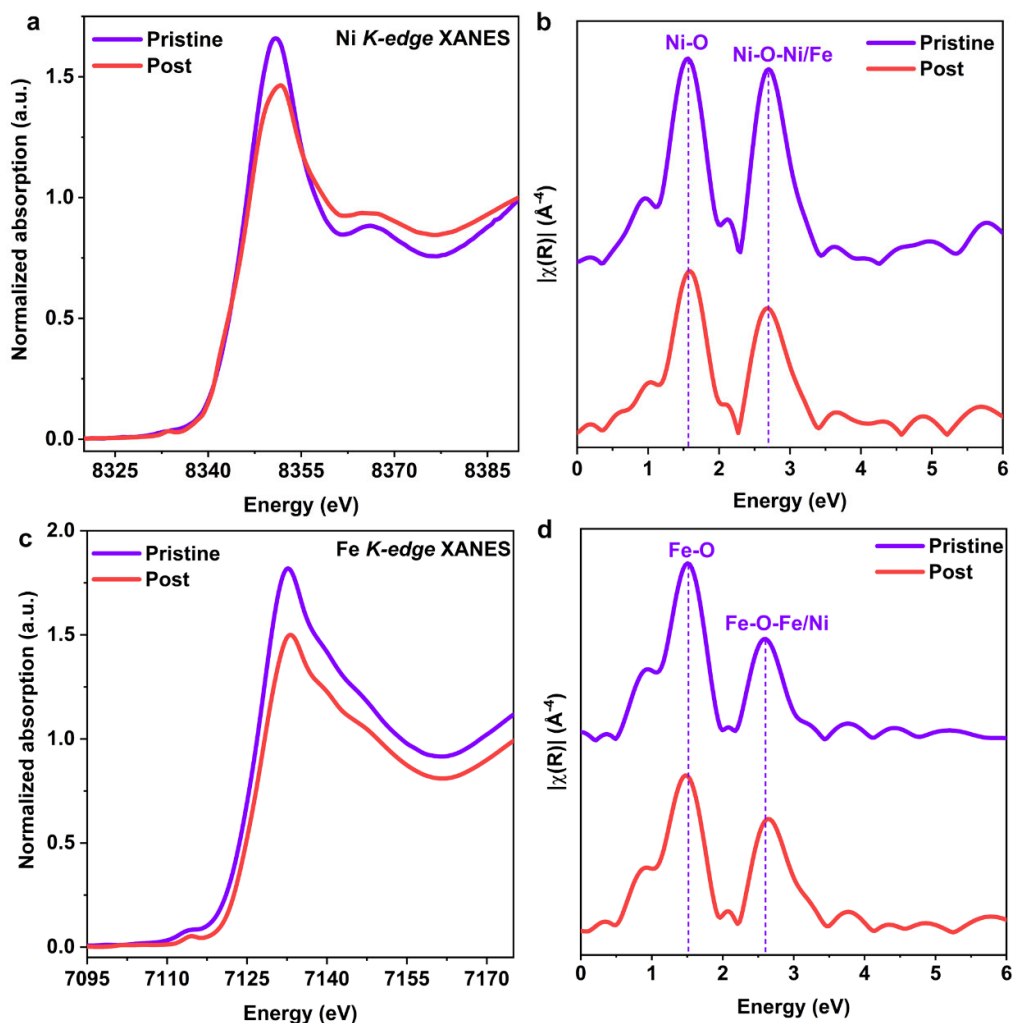


Figure S50. (a, b) Ni *K*-edge XANES and the corresponding EXAFS spectra of R-NiFe-CPs before and after OER measurements. (c, d) Fe *K*-edge XANES and the corresponding EXAFS spectra of R-NiFe-CPs before and after OER measurements.

Evaluations of the FT-EXAFS data (**Figures S50b and S50d**) revealed that all of the corresponding peaks of post-catalytic R-NiFe-CPs samples were similar to those of the pristine R-NiFe-CPs. For the Ni *K*-edge EXAFS data (**Figure S50 b**), the main coordination peak at 1.56 Å corresponds to the Ni-O bonds, and the second coordination peak at 2.69 Å is mainly due to scattering from the Ni-O-Ni/Fe bonds. The Fe *K*-edge XAS data also provided analogous evidence for the existence of Fe-O bonds and Fe-O-Fe/Ni bonds in the post-catalytic R-NiFe-CPs. Moreover, a slight negative peak shift was found for the scattering of Fe-O bonds in post R-NiFe-CPs, which was mainly due to the formation of higher valence states of Fe.^[14, 26] All the above results indicate that R-NiFe-CPs maintained their pristine structures well after the OER measurements.

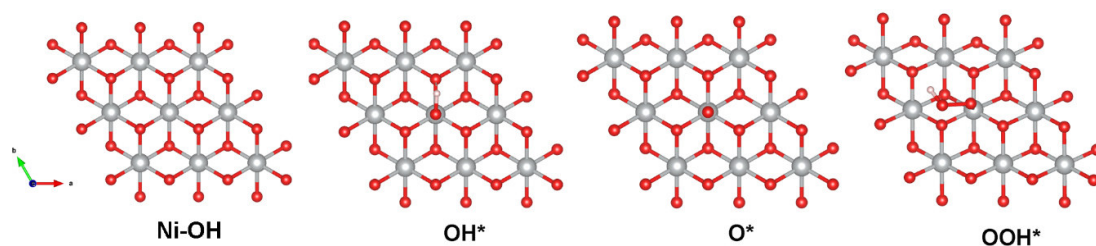


Figure S51. Adsorption slab models of Ni-OH.

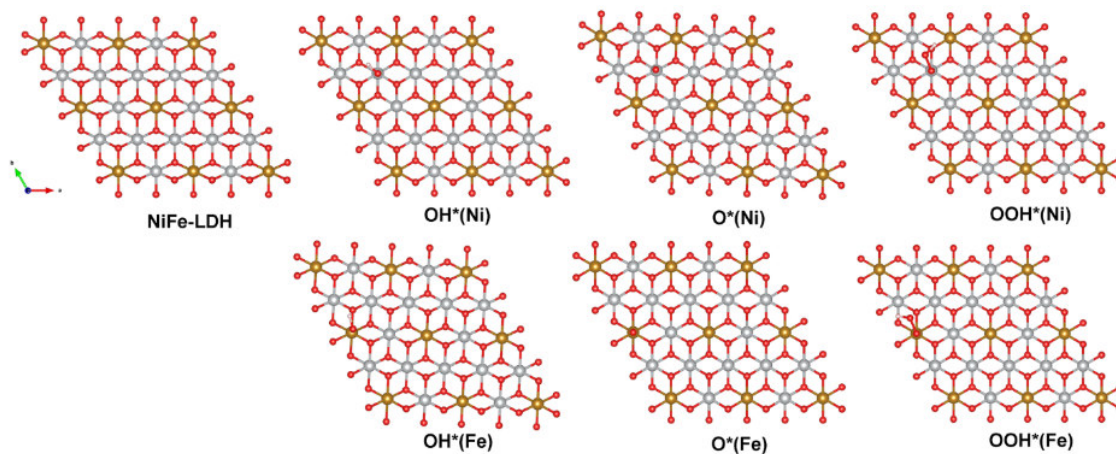


Figure S52. Adsorption slab models of NiFe-LDH.

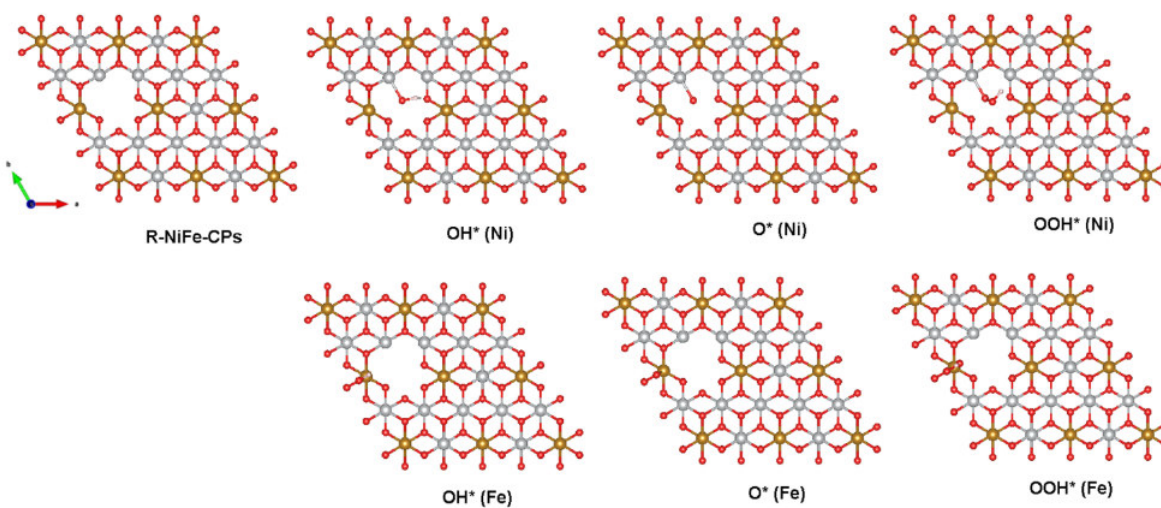


Figure S53. Adsorption slab models of R-NiFe-CPs.

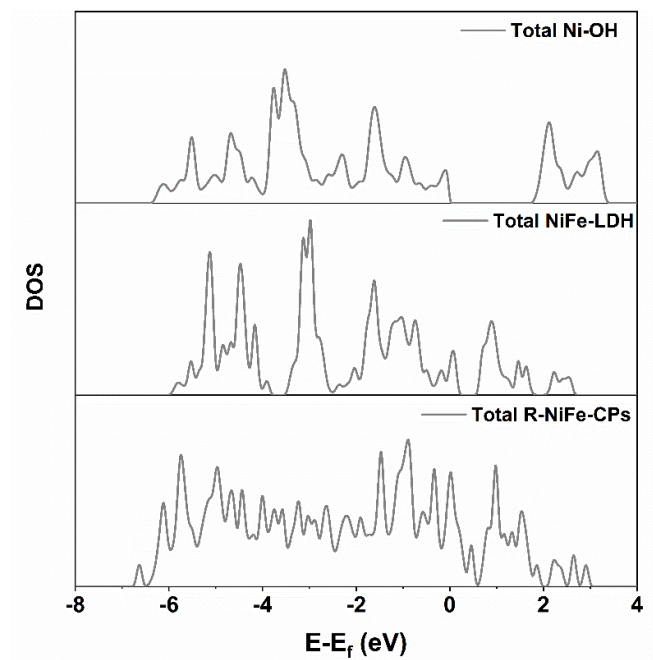


Figure S54. Computed total DOS of Ni-OH, NiFe-LDH, and R-NiFe-CPs.

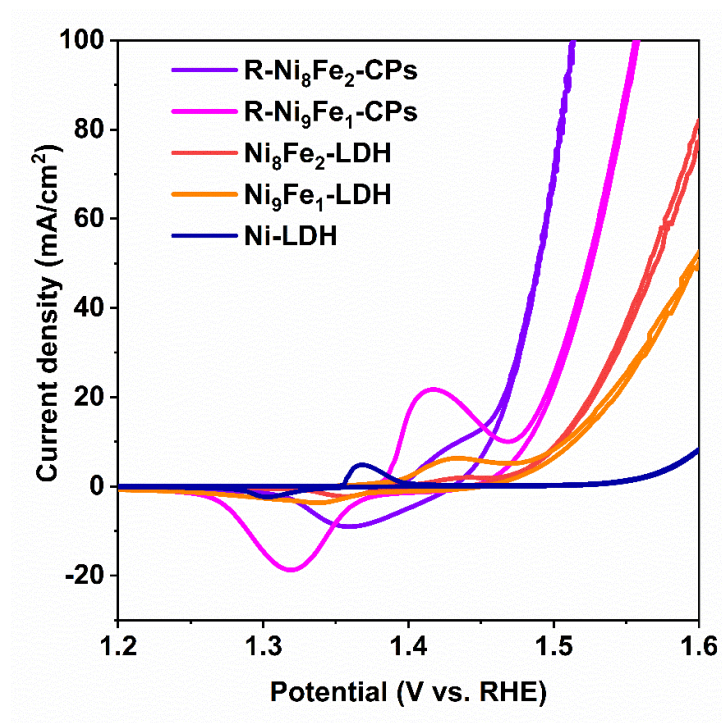


Figure S55. CV curves of R-Ni_{10-x}Fe_x-CPs and Ni_{10-x}Fe_x-LDH.

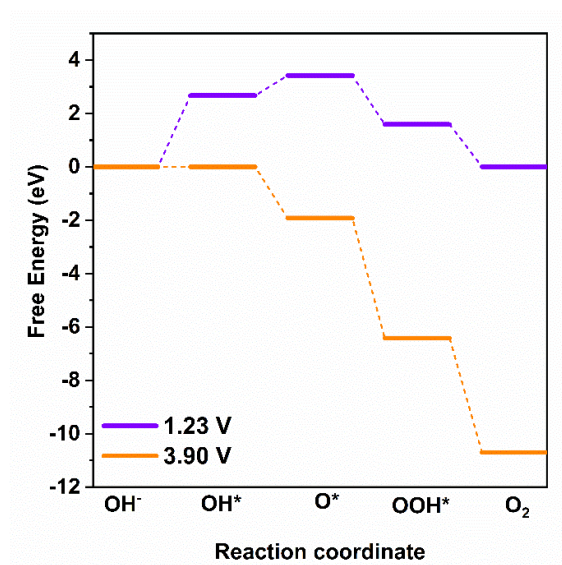


Figure S56. Computed free energies of OER steps for Ni-LDH at equilibrium potential for OER and minimum potential for which all steps become downhill.

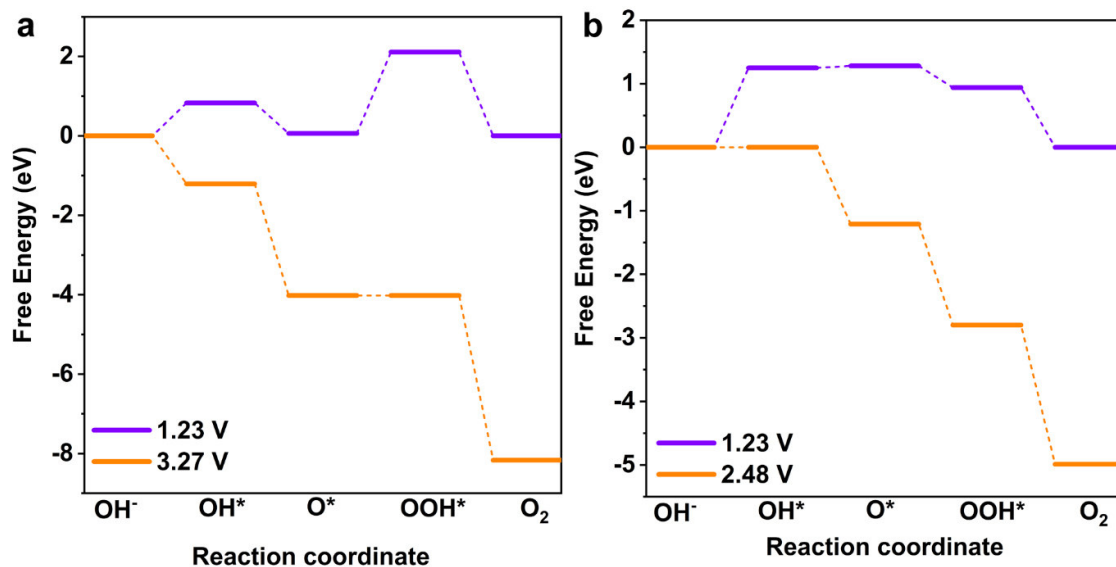


Figure S57. Computed free energies of OER steps for NiFe-LDH at equilibrium potential for OER and minimum potential for which all steps become downhill: (a) Ni site; (b) Fe site.

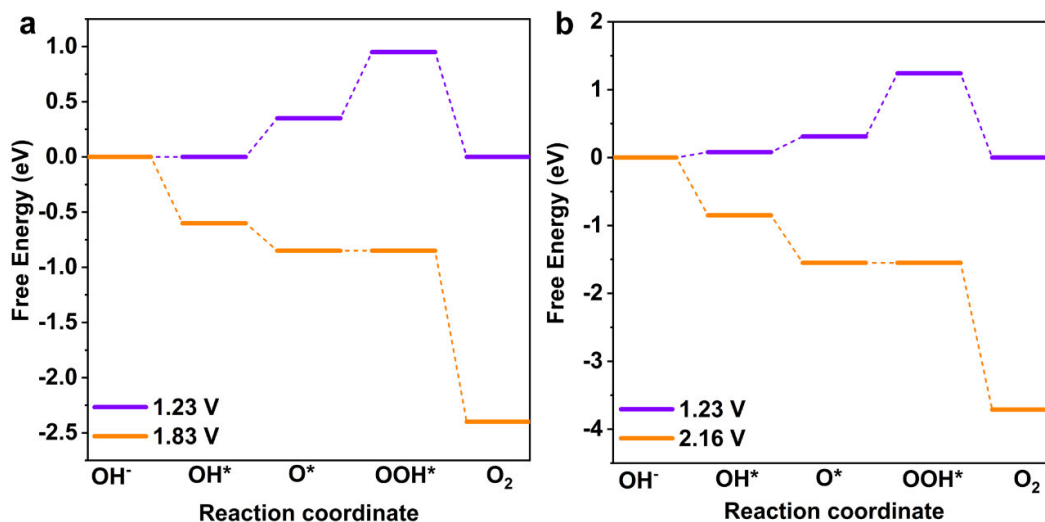


Figure S58. Computed free energies of OER steps for R-NiFe-CPs at equilibrium potential for OER and minimum potential for which all steps become downhill: (a) Ni site; (b) Fe site.

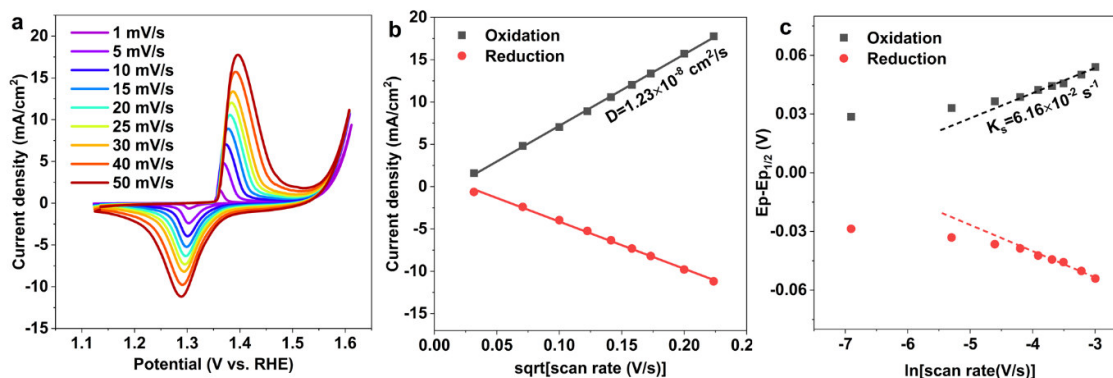


Figure S59. (a) CVs of Ni-OH with scan rate from 1 to 50 mV/s in purified 1 M KOH. (b) Redox peak current densities vs the square root of scan rates. (c) Redox peak potentials vs the logarithm of scan rates.

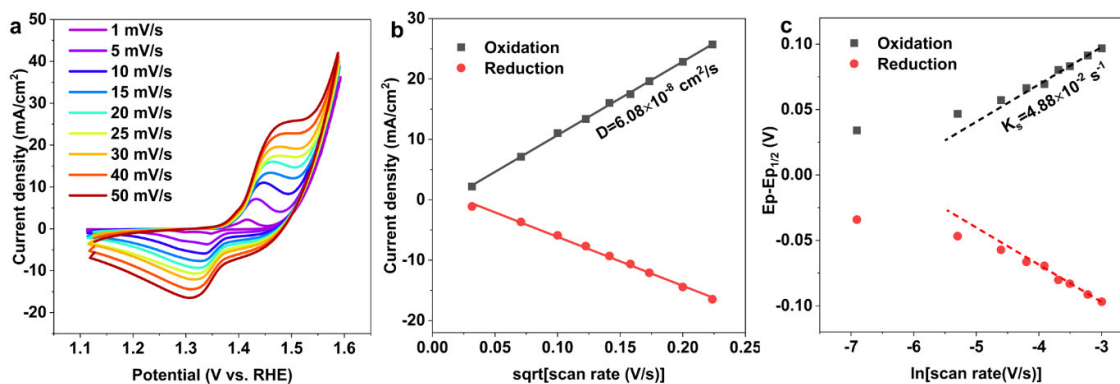


Figure S60. (a) CVs of Ni₉Fe₁-LDH with scan rate from 1 to 50 mV/s in purified 1 M KOH. (b) Redox peak current densities vs the square root of scan rates. (c) Redox peak potentials vs the logarithm of scan rates.

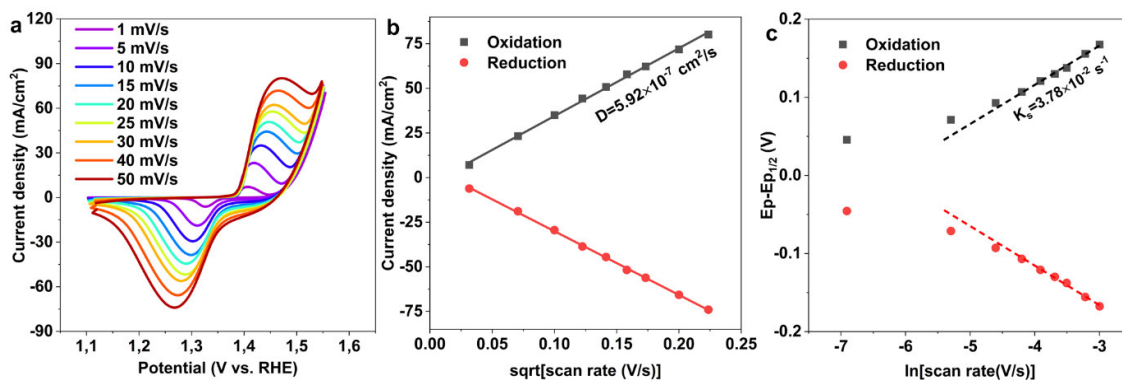


Figure S61. (a) CVs of R-Ni₉Fe₁-CPs with scan rate from 1 to 50 mV/s in purified 1 M KOH. (b) Redox peak current densities vs the square root of scan rates. (c) Redox peak potentials vs the logarithm of scan rates.

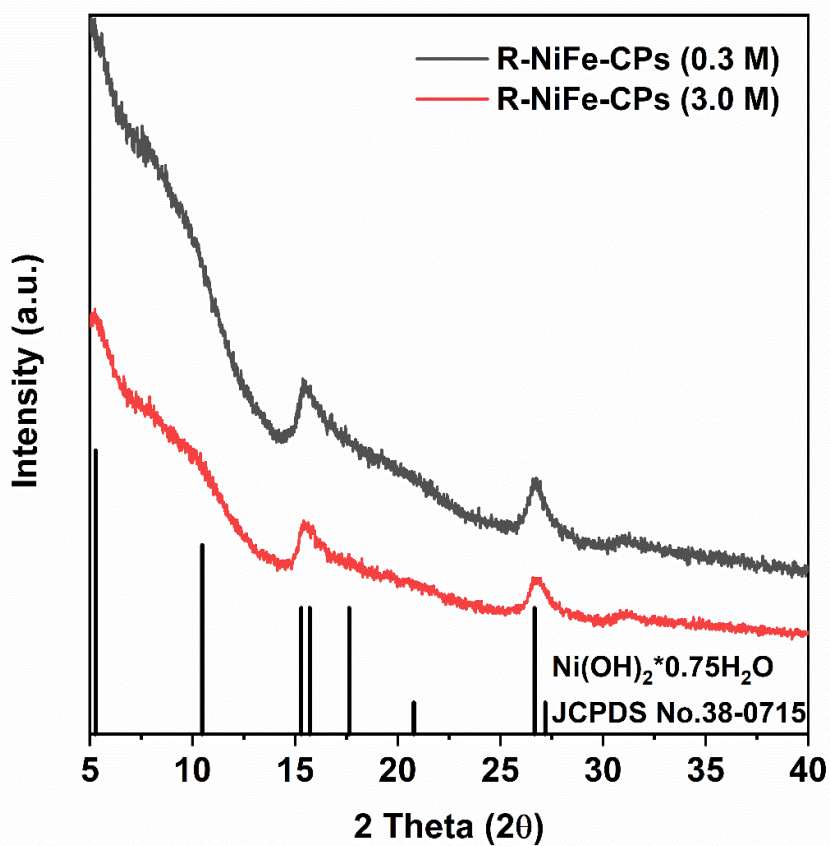


Figure S62. PXRD patterns of R-NiFe-CPs obtained with 0.3 and 3.0 M of NaBH₄.

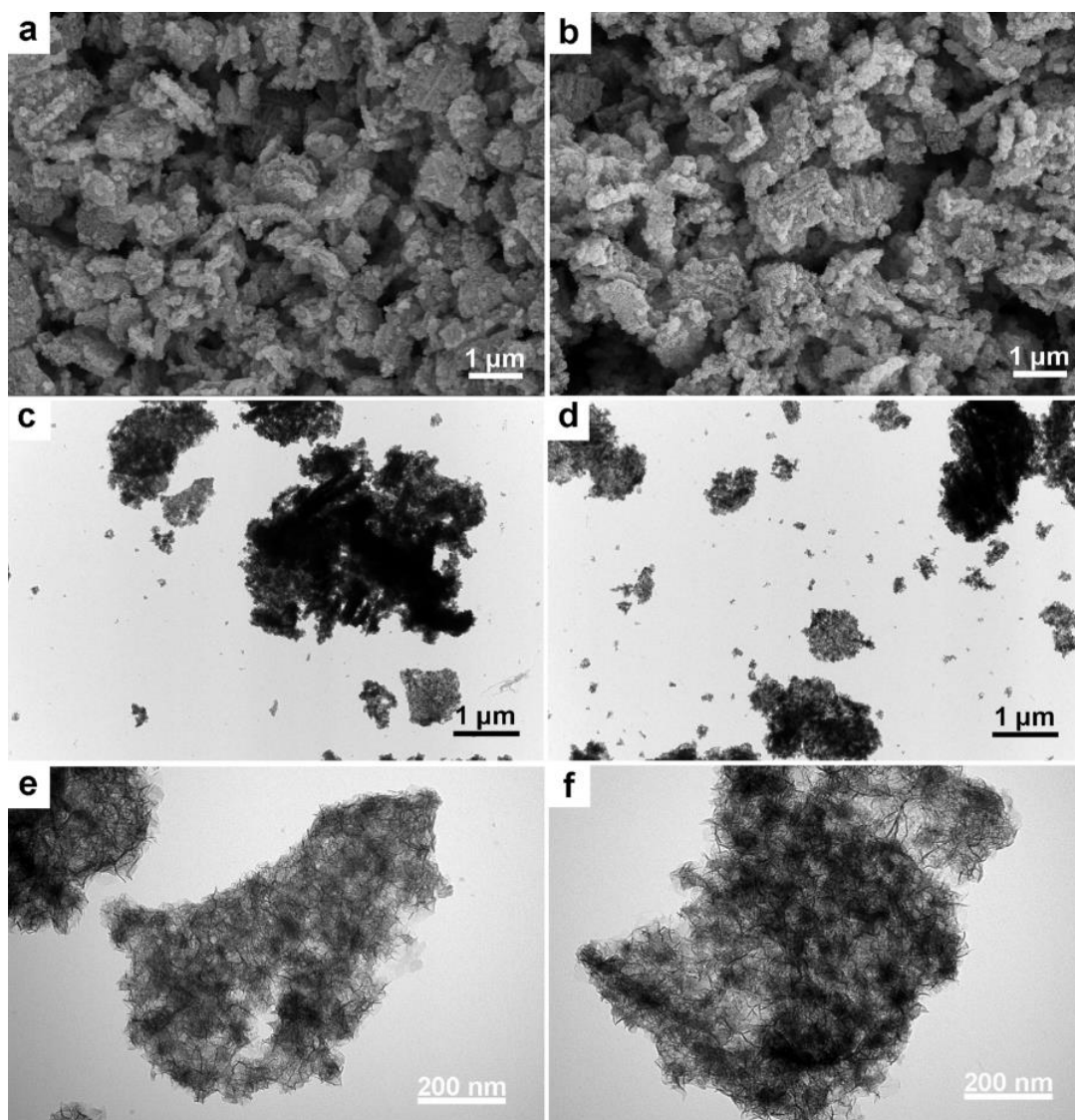


Figure S63. FESEM and TEM images of R-NiFe-CPs obtained with different concentrations of NaBH_4 : (a, c, e) 0.3 M; (b, d, f) 3.0 M.

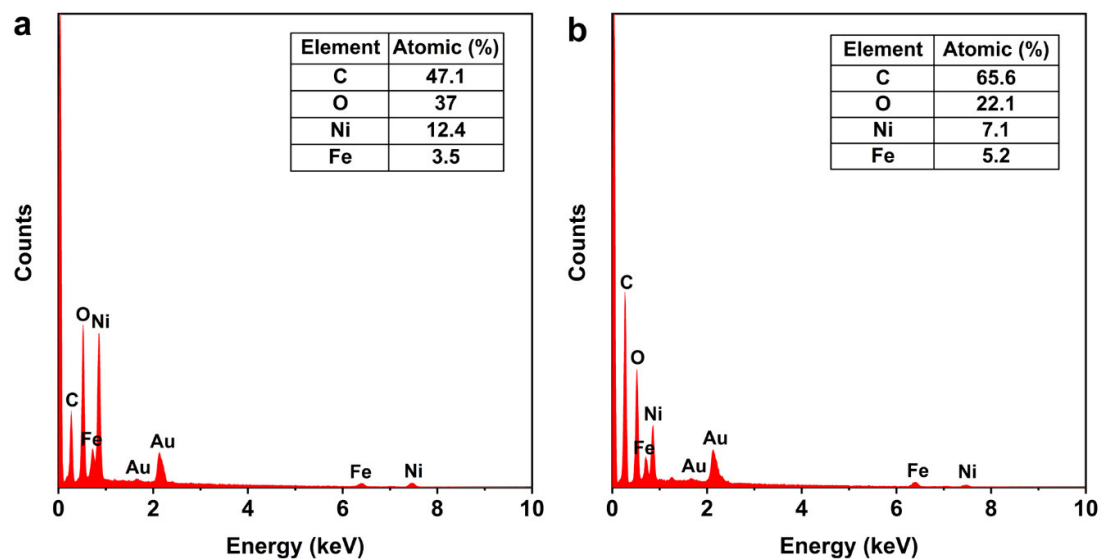


Figure S64. FESEM-EDX spectra of R-NiFe-CPs with different concentrations of NaBH₄: (a) 0.3 M; (b) 3.0 M.

The Ni/Fe atomic ratio showed an increasing trend as a function of the NaBH₄ concentration, which implies that more Ni deficiencies were formed.

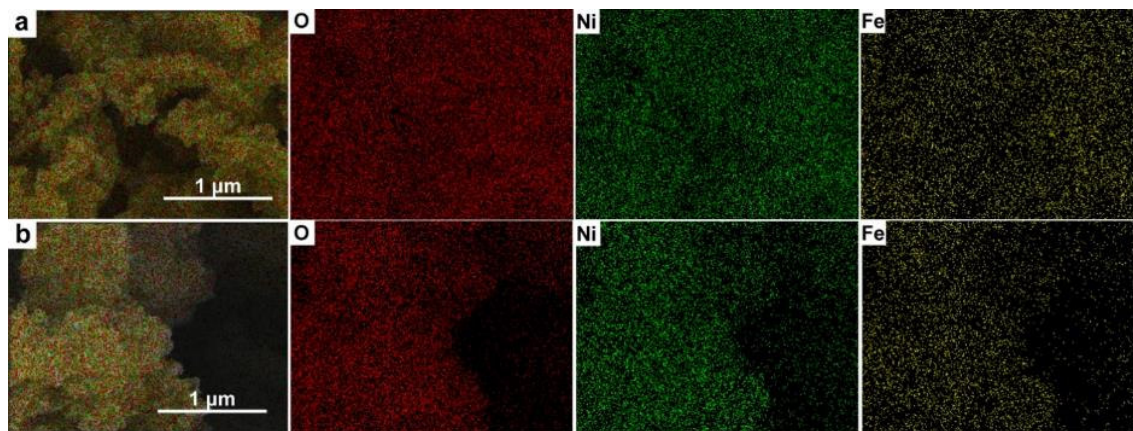


Figure S65. FESEM-EDX elemental mappings of R-NiFe-CPs with different concentrations of NaBH₄: (a) 0.3 M; (b) 3.0 M.

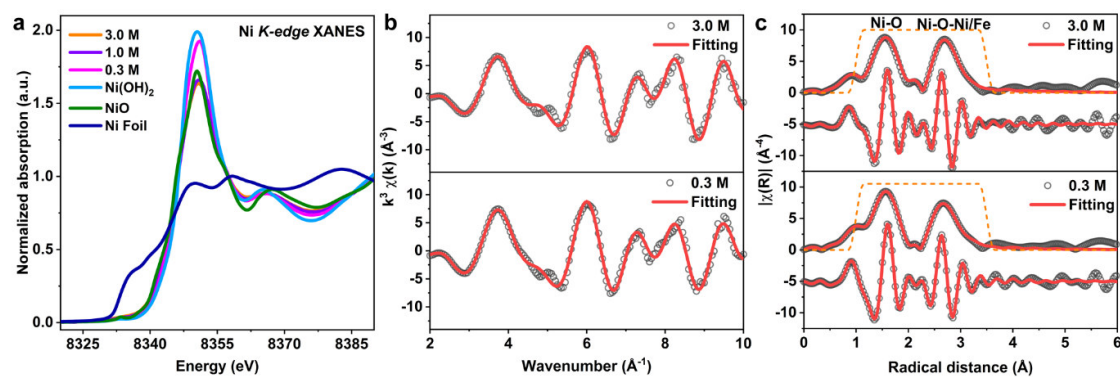


Figure S66. (a) Ni K-edge XANES spectra of R-NiFe-CPs with 0.3, 1.0, and 3.0 M of NaBH₄. (b, c) Fitting of the Ni K-edge EXAFS spectra of R-NiFe-CPs with 0.3 and 3.0 M of NaBH₄.

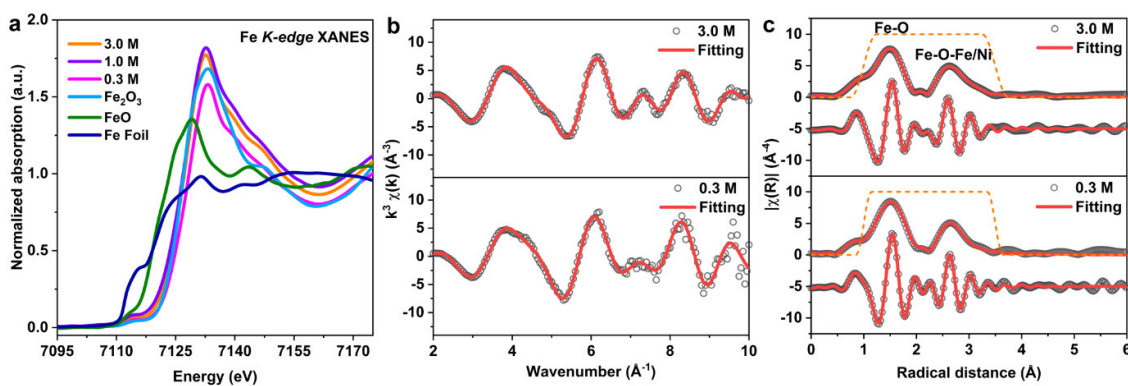


Figure S67. (a) Fe K-edge XANES of R-NiFe-CPs with 0.3, 1.0, and 3.0 M of NaBH₄. (b, c) Fitting of the Fe K-edge EXAFS of R-NiFe-CPs with 0.3 and 3.0 M of NaBH₄.

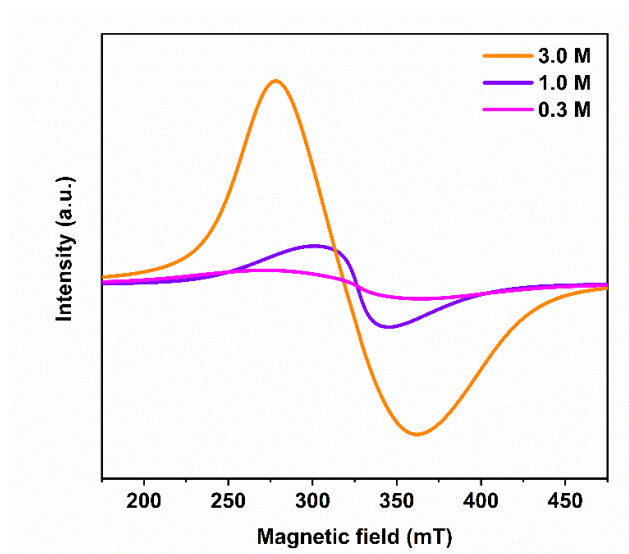


Figure S68. Room temperature EPR spectra of R-NiFe-CPs obtained with 0.3, 1.0, and 3.0 M of NaBH₄.

Table S1. ICP-MS results: Ni/Fe ratio in precipitate and solution for the synthesis of Ni₈Fe₂-CPs (referred to as NiFe-CPs).

Feeding ratio	Precipitate	Solution
4:1	3.21:1	4.87:1

Table S2. ICP-MS results: B and Na contents in the solution for the synthesis of R-Ni₈Fe₂-CPs (referred to as R-NiFe-CPs).

Elements	B (mg/mL)	Na (mg/mL)
Solution	11.41 (~1 M)	34.97
Reference DI water	6.83 ×10 ⁻³	3.65×10 ⁻²

Table S3. ICP-MS results: purified 1 M KOH before and after OER measurements.

Samples	Ni (ng/mL)	Fe (ng/mL)
Free	10.00	0.47
After measurements	8.96	0.58

Table S4. Elemental analysis of NiFe-CPs and R-NiFe-CPs.

Elements	C (mass-%)	H (mass-%)	N (mass-%)
NiFe-CPs	17.45	2.26	20.01
R-NiFe-CPs	0.98	2.57	0.90

Table S5. Ni/Fe ratio of R-NiFe-CPs, NiFe-CPs, NiFe-LDH, and NiFe-oxides, and R-NiFe-NPs based on FESEM EDX and ICP-MS results.

Samples	EDX results	ICP-MS results
R-NiFe-CPs	2.86	2.96
NiFe-CPs	3.18	3.21
NiFe-LDH	2.75	2.85
NiFe-Oxides	3.28	3.33
R-NiFe-NPs	3.07	3.21

Table S6. ICP-MS results: Ni/Fe ratio in the precipitate and solution for the synthesis of R-NiFe-CPs.

Precipitate	Solution
2.96:1	4.15:1

Table S7. Fitting parameters of Ni *K*-edge EXAFS spectra for the as-prepared catalysts and references. **CN**: coordination numbers; **R**: bond distance; σ^2 : Debye-Waller factors; **S₀²**: amplitude reduction factor).

Samples	Path	CN	R	σ^2	ΔE_0
Ni foil (S₀²=0.89)	Ni-Ni	12.00	2.490	0.0080	-4.7
Ni₅Fe₅-CPs (S₀²=0.89)	Ni-C	4.00	1.854	0.0008	-3.9
	Ni-N	4.00	3.067	0.0029	
	Ni-C-N	8.00	3.065	0.0024	
NiFe-LDH (S₀²=0.74)	Ni-O	6.04	2.039	0.0067	-4.3
	Ni-O-Ni	3.94	3.103	0.0051	
	Ni-O-Fe	2.05	3.032	0.0097	
Ni(OH)₂ (S₀²=1.25)	Ni-O	6.00	2.076	0.0080	0.1
	Ni-O-Ni	6.00	3.130	0.0078	
R-NiFe-CPs (0.3 M) (S₀²=1.25)	Ni-O	5.15	2.057	0.0080	-1.8
	Ni-O-Ni	4.02	3.138	0.0081	
	Ni-O-Fe	2.03	3.031	0.0074	
R-NiFe-CPs (1.0 M) (S₀²=1.25)	Ni-O	4.86	2.067	0.0081	-1.4
	Ni-O-Ni	3.67	3.123	0.0065	
	Ni-O-Fe	1.96	3.026	0.0098	
R-NiFe-CPs (3.0 M) (S₀²=1.25)	Ni-O	4.33	2.061	0.0067	-1.8
	Ni-O-Ni	3.34	3.127	0.0056	
	Ni-O-Fe	1.98	3.018	0.0097	
R-Ni₅Fe₅-CPs (S₀²=1.25)	Ni-O	4.27	2.070	0.0071	0.1
	Ni-O-Ni	2.05	3.154	0.0075	
	Ni-O-Fe	2.89	3.074	0.0086	

Table S8. Fitting parameters of Fe *K*-edge EXAFS spectra for the as-prepared catalysts and references (CN: coordination numbers; **R**: bond distance; σ^2 : Debye-Waller factors; S_0^2 : amplitude reduction factor).

Samples	Path	CN	R (Å)	σ^2	ΔE
Fe foil	Fe-Fe	8.00	2.448	0.0036	3.8
$S_0^2=0.91$	Fe-Fe	6.00	2.840	0.0028	
Ni₅Fes-CPs	Fe-N	4.00	2.095	0.0061	-0.4
$S_0^2=1.15$	Fe-O	2.00	2.190	0.0073	
	Fe-C	4.00	3.227	0.0030	
	Fe-N-C	8.00	3.308	0.0035	
NiFe-LDH	Fe-O	5.94	2.003	0.0099	-2.9
$S_0^2=0.80$	Fe-O-Fe	1.99	2.962	0.0147	
	Fe-O-Ni	3.88	3.055	0.0070	
R-NiFe-CPs (0.3 M)	Fe-O	5.95	2.009	0.0084	-3.2
$S_0^2=0.91$	Fe-O-Fe	2.06	2.984	0.0092	
	Fe-O-Ni	4.09	3.104	0.0080	
R-NiFe-CPs (1.0 M)	Fe-O	5.58	2.013	0.0072	-2.8
$S_0^2=0.91$	Fe-O-Fe	1.94	3.045	0.0050	
	Fe-O-Ni	3.47	3.155	0.0096	
R-NiFe-CPs (3.0 M)	Fe-O	5.26	2.014	0.0051	-2.2
$S_0^2=0.91$	Fe-O-Fe	2.01	3.084	0.0063	
	Fe-O-Ni	2.33	3.155	0.0088	
R-Ni₅Fes-CPs	Fe-O	5.25	2.006	0.0095	-2.6
$S_0^2=0.91$	Fe-O-Fe	2.81	3.053	0.0092	
	Fe-O-Ni	1.92	3.175	0.0088	

Table S9. Comparison of OER performance of the as-prepared catalysts with recent representative studies on NiFe-based OER electrocatalysts.

Electrode materials	Overpotential (mV) at 10 mA/cm ²	Tafel slope (mV/dec)	Stability (h)	Substrate	Ref.
Laminar NiFe-LDH	197	100	24 h	GC-RDE	[18]
Ni ₂ P@NiFe-LDH	205	32	15 h	Ni foam	[19]
NiFe-LDH@DG10	210	52	10 h	GC-RDE	[20]
NiFe-LDH@CNTs	220	34	18 h	GC-RDE	[21]
NiFe-LDH-V _{Ni}	229	62.9	-	GC-RDE	[14]
NiFe-LDH@graphene	230	42	10 h	GC-RDE	[22]
Defect NiFe-LDH	230	47	100 h	Graphite paper	[23]
CQD/NiFe-LDH	235	30	0.8 h	GC-RDE	[24]
Fe _{6.4} Ni _{16.1} P _{12.9} B _{4.3} O _{60.2}	236	39	50 h	GC-RDE	[25]
NiFe-LDH/CNT	247	31	60 h	Graphite paper	[26]
Fe ²⁺ -NiFe-LDH	249	40.3	15 h	Graphite paper	[27]
NiFe-LDH-VO	250	69	11 h	Ni foam	[28]
Atomic layer NiFe-LDH	254	32	12 h	Graphite paper	[29]
HPGC@NiFe-LDH	265	56	50 h	GC-RDE	[30]
NiFe-LDH/C	270	56	100 h	Graphite paper	[31]
Exfoliated NiFe-LDH	270	89	10 h	GC-RDE	[20]
NiFe-N-CNT-rGO	270	42	2 h	GC-RDE	[32]
Monolayer NiFe-LDH	272	54	-	Graphite paper	[23]
Single-layer NiFe-LDH	279	33.4	8 h	GC-RDE	[33]
NiFe-LDH	280	47.6	5 h	GC-RDE	[34]
Ultra-thin NiFe-LDH	280	46	9 h	GC-RDE	[35]
NiFe-LDH nanoprisms	280	49.4	6 h	GC-RDE	[36]
Amorphous NiFe-LDH	292	30.4	2 h	GC-RDE	[37]
NiFe-LDH NS	300	40	12 h	GC-RDE	[38]
Ni _{0.75} Fe _{0.25} (OH) _x	310	68	10 h	GC-RDE	[39]
Porous NiFe oxides	328	42	12 h	GC-RDE	[40]
NiFe-LDH/3D carbon	340	71	20 h	GC-RDE	[41]
R-NiFe-CPs	225	27.78	120 h	GC-RDE	This work
R-NiFe-NPs	251	40.69	3 h	GC-RDE	This work
NiFe-CPs	261	29.35	3 h	GC-RDE	This work
NiFe-LDH	273	50.21	3 h	GC-RDE	This work
NiFe-Oxides	300	54.52	3 h	GC-RDE	This work

Table S10. Comparison of OER performance of the as-prepared catalysts with recent representative works on ultra-thin based OER electrocatalysts.

Electrode materials	Overpotential (mV) at 10 mA/cm ²	Tafel slope (mV/dec)	Stability (h)	Substrate	Ref.
Amorphous PVP/CoFe _{1.3}	230	47.4	14 h	Ni foam	[42]
Ni-ZIF/Ni-B	234	57	36 h	Ni foam	[43]
NiFe-MOF array	240	34	5.5 h	Ni foam	[44]
NiCo-UMOFNs	250	42	200 h	GC-RDE	[45]
CoV-UAH	250	44	120 h	Au foam	[46]
CoOOH-NS	253	39	12 h	Graphite paper	[47]
O-NFS-ECT	259 at 20 mA/cm ²	69	11 h	Ni foam	[48]
Fe-Mn-O NSs	265	63.9	12 h	Graphite paper	[49]
Ultrathin Ni/Ni(OH) ₂	270	70	10 h	Ni foam	[50]
LM-160-12	274	44.7	10 h	GC-RDE	[51]
CoFe ₂ O ₄ NSs	275	42.1	10 h	GC-RDE	[52]
CoSe ₂ UNM _{vac}	284	46.3	20 h	GC-RDE	[53]
Ni _{0.3} Co _{0.7} -9AC-AD/N	320 at 50 mA/cm ²	51.3	30 h	Ni foam	[54]
1 nm CoO _x	360	76	0.8 h	GC-RDE	[55]
R-NiFe-CPs	225	27.78	120 h	GC-RDE	This work
R-NiFe-NPs	251	40.69	3 h	GC-RDE	This work
NiFe-CPs	261	29.35	3 h	GC-RDE	This work
NiFe-LDH	273	50.21	3 h	GC-RDE	This work
NiFe-Oxides	300	54.52	3 h	GC-RDE	This work

References

- [1] A. Garron, D. Swierczynski, S. Bennici, A. Auroux, *Int. J. Hydrog. Energy* **2009**, *34*, 1185.
- [2] Z. Lu, W. Xu, W. Zhu, Q. Yang, X. Lei, J. Liu, Y. Li, X. Sun, X. Duan, *Chem. Commun.* **2014**, *50*, 6479.
- [3] R. Gao, D. Yan, *Adv. Energy Mater.* **2020**, *10*, 1900954.
- [4] L. Trotochaud, S. L. Young, J. K. Ranney, S. W. Boettcher, *J. Am. Chem. Soc.* **2014**, *136*, 6744.
- [5] I. Spanos, M. F. Tesch, M. Yu, H. Tüysüz, J. Zhang, X. Feng, K. Müllen, R. Schlögl, A. K. Mechler, *ACS Catalysis* **2019**, *9*, 8165.
- [6] R. Farhat, J. Dhainy, L. I. Halaoui, *ACS Catalysis* **2020**, *10*, 20.
- [7] T. Ma, S. Dai, M. Jaroniec, S. Qiao, *J. Am. Chem. Soc.* **2014**, *136*, 13925.
- [8] Y. Zhao, C. K. Mavrokefalos, P. Zhang, R. Erni, J. Li, C. A. Triana, G. R. Patzke, *Chem. Mater.* **2020**, *32*, 1371.
- [9] R.G. Compton, C.E. Banks, *Understanding Voltammetry*, 2nd ed., Imperial College Press, UK **2011**.
- [10] E. Laviron, *J. Electroanal. Chem.* **1979**, *100*, 263.
- [11] J. Wang, L. Gan, W. Zhang, Y. Peng, H. Yu, Q. Yan, X. Xia, X. Wang, *Sci. Adv.* **2018**, *4*, eaap7970.
- [12] V. I. Anisimov, F. Aryasetiawan, A. Lichtenstein, *J. Phys. Condens. Matter* **1997**, *9*, 767.
- [13] V. I. Anisimov, J. Zaanen, O. K. Andersen, *Phys. Rev. B* **1991**, *44*, 943.
- [14] Y. Wang, M. Qiao, Y. Li, S. Wang, *Small* **2018**, *14*, 1800136.
- [15] Q. He, Y. Wan, H. Jiang, Z. Pan, C. Wu, M. Wang, X. Wu, B. Ye, P. M. Ajayan, L. Song, *ACS Energy Letters* **2018**, *3*, 1373.
- [16] Á. Valdés, Z.-W. Qu, G.-J. Kroes, J. Rossmeisl and J. K. Nørskov, *J. Phys. Chem. C* **2008**, *112*, 9872.
- [17] T. Kitazawa, M. Fukunaga, M. Takahashi, M. Takeda, *Mol. Cryst. Liq. Cryst.* **1994**, *244*, 331.
- [18] H. Zhang, H. Li, B. Akram, X. Wang, *Nano Res.* **2019**, *12*, 1327.
- [19] F.-S. Zhang, J.-W. Wang, J. Luo, R.-R. Liu, Z.-M. Zhang, C.-T. He, T.-B. Lu, *Chem. Sci.* **2018**, *9*, 1375.
- [20] Y. Jia, L. Zhang, G. Gao, H. Chen, B. Wang, J. Zhou, M. T. Soo, M. Hong, X. Yan, G. Qian, J. Zou, A. Du, X. Yao, *Adv. Mater.* **2017**, *29*, 1700017.
- [21] D. Zhao, K. Jiang, Y. Pi, X. Huang, *ChemCatChem* **2017**, *9*, 84.
- [22] W. Ma, R. Ma, C. Wang, J. Liang, X. Liu, K. Zhou, T. Sasaki, *ACS Nano* **2015**, *9*, 1977.
- [23] X. Zhang, Y. Zhao, Y. Zhao, R. Shi, G. I. N. Waterhouse, T. Zhang, *Adv. Energy Mater.* **2019**, *9*, 1900881.
- [24] Di Tang, J. Liu, X. Wu, R. Liu, X. Han, Y. Han, H. Huang, Y. Liu, Z. Kang, *ACS Appl. Mater. Interfaces* **2014**, *6*, 7918.
- [25] H. Ren, X. Sun, C. Du, J. Zhao, D. Liu, W. Fang, S. Kumar, R. Chua, S. Meng, P. Kidkhunthod, L. Song, S. Li, S. Madhavi, Q. Yan, *ACS Nano* **2019**, *13*, 12969.
- [26] M. Gong, Y. Li, H. Wang, Y. Liang, J. Z. Wu, J. Zhou, J. Wang, T. Regier, F. Wei, H. Dai, *J. Am. Chem. Soc.* **2013**, *135*, 8452.
- [27] Z. Cai, D. Zhou, M. Wang, S.-M. Bak, Y. Wu, Z. Wu, Y. Tian, X. Xiong, Y. Li, W. Liu, S. Siahrostami, Y. Kuang, X.-Q. Yang, H. Duan, Z. Feng, H. Wang, X. Sun, *Angew. Chem. Int. Ed.* **2018**, *57*, 9392; *Angew. Chem.* **2018**, *130*, 9536.
- [28] D. Zhou, X. Xiong, Z. Cai, N. Han, Y. Jia, Q. Xie, X. Duan, T. Xie, X. Zheng, X. Sun, X. Duan, *Small Methods* **2018**, *2*, 1800083.
- [29] Y. Zhao, X. Zhang, X. Jia, G. I. N. Waterhouse, R. Shi, X. Zhang, F. Zhan, Y. Tao, L.-Z. Wu, C.-H. Tung, D. O'Hare, T. Zhang, *Adv. Energy Mater.* **2018**, *8*, 1703585.
- [30] Y. Ni, L. Yao, Y. Wang, B. Liu, M. Cao, C. Hu, *Nanoscale* **2017**, *9*, 11596.
- [31] C. Andronesco, S. Barwe, E. Ventosa, J. Masa, E. Vasile, B. Konkena, S. Möller, W. Schuhmann, *Angew. Chem. Int. Ed.* **2017**, *56*, 11258; *Angew. Chem.* **2017**, *129*, 11411.
- [32] W. Wan, S. Wei, J. Li, C. A. Triana, Y. Zhou, G. R. Patzke, *J. Mater. Chem. A* **2019**, *7*, 15145.
- [33] R. Gao, D. Yan, *Nano Res.* **2018**, *11*, 1883.
- [34] B. M. Hunter, J. D. Blakemore, M. Deimund, H. B. Gray, J. R. Winkler, A. M. Müller, *J. Am. Chem. Soc.* **2014**, *136*, 13118.
- [35] X. Jia, Y. Zhao, G. Chen, L. Shang, R. Shi, X. Kang, G. I. N. Waterhouse, L.-Z. Wu, C.-H. Tung, T. Zhang, *Adv. Energy Mater.* **2016**, *6*, 1502585.
- [36] Le Yu, J. F. Yang, B. Y. Guan, Y. Lu, X. W. Lou, *Angew. Chem. Int. Ed.* **2018**, *57*, 172; *Angew. Chem.* **2018**, *130*, 178.
- [37] E. Lee, A.-H. Park, H.-U. Park, Y.-U. Kwon, *Ultrason. Sonochem.* **2018**, *40*, 552.
- [38] F. Song, X. Hu, *Nat. Commun.* **2014**, *5*, 4477.
- [39] T. Tian, M. Zheng, J. Lin, X. Meng, Y. Ding, *Chem. Commun.* **2019**, *55*, 1044.
- [40] J. Qi, W. Zhang, R. Xiang, K. Liu, H.-Y. Wang, M. Chen, Y. Han, R. Cao, *Adv. Sci.* **2015**, *2*, 1500199.
- [41] W. Wang, Y. Liu, J. Li, J. Luo, L. Fu, S. Chen, *J. Mater. Chem. A* **2018**, *6*, 14299.
- [42] Z. Guo, W. Ye, X. Fang, J. Wan, Y. Ye, Y. Dong, D. Cao, D. Yan, *Inorg. Chem. Front.* **2019**, *6*, 687.

- [43] H. Xu, B. Fei, G. H. Cai, Y. Ha, J. Liu, H. X. Jia, J. Zhang, M. Liu, R. Wu, *Adv. Energy Mater.* **2020**, *10*, 1902714.
- [44] J. Duan, S. Chen, C. Zhao, *Nat. Commun.* **2017**, *8*, 15341.
- [45] S. Zhao, Y. Wang, J. Dong, C.-T. He, H. Yin, P. An, K. Zhao, X. Zhang, C. Gao, L. Zhang, J. Lv, J. Wang, J. Zhang, A. M. Khatkhat, N. A. Khan, Z. Wei, J. Zhang, S. Liu, H. Zhao, Z. Tang, *Nat. Energy* **2016**, *1*, 16184.
- [46] J. Liu, Y. Ji, J. Nai, X. Niu, Y. Luo, L. Guo, S. Yang, *Energy Environ. Sci.* 2018, **11**, 1736.
- [47] J. Zhou, Y. Wang, X. Su, S. Gu, R. Liu, Y. Huang, S. Yan, J. Li, S. Zhang, *Energy Environ. Sci.* **2019**, *12*, 739.
- [48] J. Zhang, Y. Hu, D. Liu, Y. Yu, B. Zhang, *Adv. Sci.* **2017**, *4*, 1600343.
- [49] Y. Teng, X.-D. Wang, J.-F. Liao, W.-G. Li, H.-Y. Chen, Y.-J. Dong, D.-B. Kuang, *Adv. Funct. Mater.* **2018**, *28*, 1802463.
- [50] L. Dai, Z.-N. Chen, L. Li, P. Yin, Z. Liu, H. Zhang, *Adv. Mater.* **2020**, *32*, 1906915.
- [51] M. Cai, Q. Liu, Z. Xue, Y. Li, Y. Fan, A. Huang, M. Li, M. Croft, T. A. Tyson, Z. Ke, G. Li, *J. Mater. Chem. A* **2020**, *8*, 190.
- [52] H. Fang, T. Huang, D. Liang, M. Qiu, Y. Sun, S. Yao, J. Yu, M. M. Dinesh, Z. Guo, Y. Xia and S. Mao, *J. Mater. Chem. A* **2019**, *7*, 7328.
- [53] Y. Zhang, C. Zhang, Y. Guo, D. Liu, Y. Yu, B. Zhang, *J. Mater. Chem. A* **2019**, *7*, 2536.
- [54] W. Ye, Y. Yang, X. Fang, M. Arif, X. Chen, D. Yan, *ACS Sustainable Chem. Eng.* **2019**, *7*, 18085.
- [55] T. P. Zhou, W. F. Xu, N. Zhang, Z. Y. Du, C. A. Zhong, W. S. Yan, H. X. Ju, W. S. Chu, H. Jiang, C. Z. Wu, Y. Xie, *Adv. Mater.* **2019**, *31*, 1807468.